RESEARCH ARTICLE

Increased RNA and Protein Degradation Is Required for Counteracting Transcriptional Burden and Proteotoxic Stress in Human Aneuploid Cells

Marica Rosaria Ippolito[1], Johanna Zerbib[2], Yonatan Eliezer[2], Eli Reuveni[2], Sonia Viganò[1], Giuseppina De Feudis[1], Eldad D. Shulman[3], Anouk Savir Kadmon[2], Rachel Slutsky[2], Tiangen Chang[3], Emma M. Campagnolo[3], Silvia Taglietti[1], Simone Scorzoni[1], Sara Gianotti[1], Sara Martin[1], Julia Muenzner[4], Michael Mülleder[5], Nir Rozenblum[2], Carmela Rubolino[6], Tal Ben-Yishay[2,7], Kathrin Laue[2], Yael Cohen-Sharir[2], Ilaria Vigorito[1], Francesco Nicassio[6], Eytan Ruppin[3], Markus Ralser[4,8,9], Francisca Vazquez[10], Stefano Santaguida[1,11], and Uri Ben-David[2]

ABSTRACT Aneuploidy results in a stoichiometric imbalance of protein complexes that jeopardizes cellular fitness. Aneuploid cells thus need to compensate for the imbalanced DNA levels by regulating their RNA and protein levels, but the underlying molecular mechanisms remain unknown. In this study, we dissected multiple diploid *versus* aneuploid cell models. We found that aneuploid cells cope with transcriptional burden by increasing several RNA degradation pathways, and are consequently more sensitive to the perturbation of RNA degradation. At the protein level, aneuploid cells mitigate proteotoxic stress by reducing protein translation and increasing protein degradation, rendering them more sensitive to proteasome inhibition. These findings were recapitulated across hundreds of human cancer cell lines and primary tumors, and aneuploidy levels were significantly associated with the response of patients with multiple myeloma to proteasome inhibitors. Aneuploid cells are therefore preferentially dependent on several key nodes along the gene expression process, creating clinically actionable vulnerabilities in aneuploid cells.

SIGNIFICANCE: Aneuploidy is a hallmark of cancer that is associated with poor prognosis and worse drug response. We reveal that cells with extra chromosomes compensate for their imbalanced DNA content by altering their RNA and protein metabolism, rendering them more sensitive to perturbation of RNA and protein degradation.

See related commentary by Bakhoum, p. 2315

INTRODUCTION

Aneuploidy is a genomic state characterized by chromosome gains and losses. A major consequence of aneuploidy is genome and proteome imbalance, which aneuploid cells must overcome in order to function properly. The degree of gene dosage compensation varies across different cellular contexts (1), yet it is clear that in human aneuploid cancer cells, the effect of aneuploidy is attenuated by such buffering mechanisms. Recent studies have revealed that many proteins do not change their expression to the degree expected based on their DNA levels (2–6). The mechanisms that allow for dosage compensation, as well as the potential cellular vulnerabilities that result from them, remain underexplored.

Previous studies have exposed the role of protein regulation and protein degradation in "buffering" the effect of copy-number alterations. Aneuploid cells experience proteotoxic stress, which is partly overcome in aneuploid yeast by an increased activity of the proteasome (7–10). Similarly, a recent study described a protein-folding deficiency in engineered aneuploid human cells (2). However, the role of the proteasome in the context of aneuploid human cancer cells has remained unknown and is of particular clinical relevance given that proteasome inhibitors are used in the clinic (mostly for treating multiple myeloma). It also remains unknown whether other important processes of protein metabolism, such as protein translation, are dysregulated in aneuploid cells.

Gene expression is also regulated at earlier stages by mRNA regulation. Although dosage compensation at the mRNA level is minimal in yeast (7, 11, 12), it does occur in human cancer cells (4, 5, 13). Recent analyses show that ~20% of genes in cancer cell lines and primary tumors do not scale with chromosome arm copy number levels (4, 13). However, the potential role of RNA transcription, metabolism, and degradation in attenuating aneuploidy-induced gene expression changes—and whether this can create cellular vulnerabilities in aneuploid cells—have yet to be explored.

In our companion study, we established a library of stable RPE1 clones with various degrees of aneuploidy (14). Here, we analyzed genomic and functional data from these isogenic clones and uncovered an increased vulnerability of aneuploid cells to perturbation of RNA and protein degradation pathways. These novel aneuploidy-induced functional dependencies were validated in human cancer cell lines, and

[1]Department of Experimental Oncology at IEO, European Institute of Oncology IRCCS, Milan, Italy. [2]Department of Human Molecular Genetics and Biochemistry, Faculty of Medicine, Tel Aviv University, Tel Aviv, Israel. [3]Cancer Data Science Laboratory, Center for Cancer Research, National Cancer Institute, National Institutes of Health, Bethesda, Maryland. [4]Department of Biochemistry, Charité Universitätsmedizin Berlin, Berlin, Germany. [5]Charité Universitätsmedizin Berlin, Core Facility High-Throughput Mass Spectrometry, Berlin, Germany. [6]Center for Genomic Science of IIT@SEMM, Fondazione Istituto Italiano di Tecnologia, Milan, Italy. [7]The Blavatnik School of Computer Science, Faculty of Exact Sciences, Tel Aviv University, Tel Aviv, Israel. [8]Nuffield Department of Medicine, University of Oxford, Oxford, United Kingdom. [9]Max Planck Institute for Molecular Genetics, Berlin, Germany. [10]Broad Institute of MIT and Harvard, Cambridge, Massachusetts. [11]Department of Oncology and Hemato-Oncology, University of Milan, Milan, Italy.

M.R. Ippolito and J. Zerbib equally contributed as a first author for this article.

S. Santaguida and U. Ben-David equally contributed as a last author for this article.

Corresponding Authors: Stefano Santaguida, Department of Experimental Oncology, European Institute of Oncology, Via Adamello 16, Milan 20139, Italy. E-mail: Stefano.santaguida@ieo.it; and Uri Ben-David, Faculty of Medicine, Room 728, Tel Aviv University, POB 39040, Ramat Aviv, Tel Aviv 69978, Israel. E-mail: ubendavid@tauex.tau.ac.il

Cancer Discov 2024;14:2532–53

doi: 10.1158/2159-8290.CD-23-0309

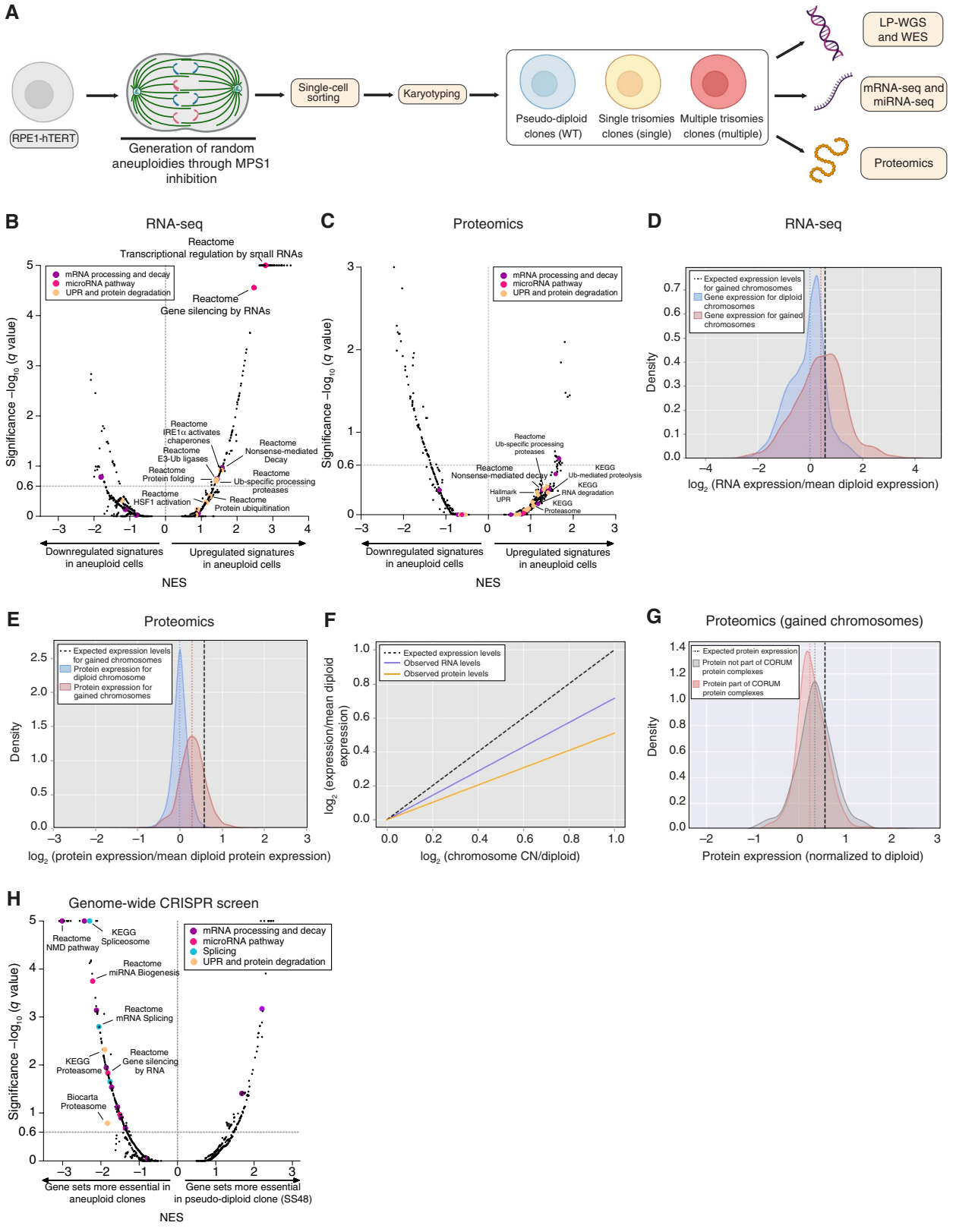

Figure 1. Dosage compensation in trisomic cells occurs at both mRNA and protein levels. **A,** Schematic representation of clone generation. See Zerbib and colleagues (14) for more details. **B,** Comparison of the differential gene expression patterns (preranked GSEA results) between the pseudo-diploid SS48 clone (control) and the highly aneuploid SS51 and SS111 clones. Plot presents enrichments for the Hallmark, KEGG, Biocarta, and Reactome gene sets. Transcriptomic data are obtained from Zerbib and colleagues (14). Significance threshold set at *q*-value = 0.25. (*continued on following page*)

differential activity of these pathways was confirmed in primary human tumors. These findings may thus have important clinical ramifications, both for the development of novel cancer therapeutics and for predicting patients' response to existing drugs.

RESULTS

Dosage Compensation in Trisomic Cells Occurs at both mRNA and Protein Levels

To investigate dosage compensation in aneuploid cells, we used a novel isogenic system of non-transformed chromosomally stable aneuploid cells, presented in detail in our companion study (14). Briefly, we transiently treated RPE1-hTERT cells with the MPS1 inhibitor reversine to induce chromosome missegregation and generate aneuploidy (15, 16), single-cell sorted and karyotyped the obtained clones [Fig. 1A; Zerbib and colleagues (14)]. RPE1-hTERT clones carry a chromosome 10q amplification as a clonal event of the parental cell line. This event is therefore shared by all the RPE1 clones, and we termed the parental and the control clones as "pseudo-diploid." We selected seven clones with increasing degrees of aneuploidy: three pseudo-diploid clones, RPE1-SS48, RPE1-SS31, and RPE1-SS77 (hereinafter SS48, SS31, and SS77, respectively); two clones carrying a single extra chromosome, RPE1-SS6 and RPE1-SS119 (hereinafter SS6 and SS119, respectively); and two clones carrying multiple trisomies, RPE1-SS51 and RPE1-SS111 (hereinafter SS51 and SS111, respectively). We identified a p53-inactivating mutation in the SS77 clone (14) and therefore used it as a *TP53*-mutant control, whereas the SS48 and SS31 clones were used as *TP53*-WT pseudo-diploid controls throughout the study. We characterized the clones extensively, demonstrating their high relevance for aneuploidy research (14).

We first investigated the gene expression differences between the pseudo-diploid and aneuploid RPE1 clones, using genome-wide RNA sequencing (RNA-seq) and mass spectrometry–based proteomics. As our aneuploid RPE1 clones harbor different trisomies, we then applied gene set enrichment analysis [GSEA (17)] to identify gene expression signatures that are induced by aneuploidy regardless of the specific affected chromosome(s). We found upregulation of signatures associated with RNA and protein regulation in aneuploid clones (Fig. 1B and C; Supplementary Fig. S1A; Supplementary Tables S1–S3). Specifically, we identified a significant upregulation of signatures related to RNA metabolism and gene silencing, e.g., "nonsense-mediated decay" and "gene silencing by RNAs" (Fig. 1B and C; Supplementary Fig. S1A), and to the unfolded protein response (UPR) and protein degradation, e.g., "IRE1α activates chaperones" and "E3-Ub ligases ubiquitinate target proteins" (Fig. 1B and C; Supplementary Fig. S1A). These results suggest global attenuation of gene and protein expression in the trisomic clones, consistent with previous studies (3, 4, 18–20).

Therefore, we set out to evaluate dosage compensation at both the mRNA and protein levels. Indeed, we found that the RNA and protein expression levels did not scale linearly with the DNA content (Fig. 1D–F). Interestingly, the correlation between the DNA and protein content was lower than that between the DNA and RNA content, in line with a greater degree of dosage compensation at the protein level (4, 18, 20). Nonetheless, in contrast to a previous report in yeast (18), we also found evidence for significant dosage compensation at the mRNA level (Fig. 1D–F). Genes that reside on gained chromosomes and encode for proteins that participate in protein complexes exhibited more dosage compensation, in comparison with genes that reside on the same chromosomes but do not belong to any protein complex—the protein abundance of such genes scaled with their DNA content to a lesser degree (Fig. 1G; Supplementary Fig. S1B). We conclude that dosage compensation is characteristic of trisomic cells, and is particularly important for protein complexes.

Therefore, we set out to identify genes that are preferentially essential in aneuploid cells, using genome-wide CRISPR–Cas9 screens of the isogenic RPE1 clones (14). Consistent with their gene expression profiles, unbiased pre-ranked GSEA revealed that aneuploid clones were more dependent on mechanisms of RNA degradation, and in particular on genes related to gene silencing through RNA processing and decay, including the nonsense-mediated decay (NMD) pathway, the miRNA pathway, and gene splicing (Fig. 1H). Indeed, the increased levels of DNA damage that we identified in the aneuploid clones (14) might result in an excessive number of abnormal transcripts, potentially explaining why aneuploid cells would be more dependent

Figure 1. ***(Continued)*** Enriched pathways are color-coded. **C,** Comparison of the differential protein expression pattern (GSEA results) between pseudo-diploid clones SS48 and SS31, and aneuploid clones SS6, SS119, SS51, and SS111. Plot presents enrichment for Hallmark, KEGG, and Reactome gene sets. Proteomics data are obtained from Zerbib and colleagues (14). Significance threshold set at *q*-value = 0.25. Enriched pathways are color-coded. **D,** Density plots of the mRNA expression from diploid (blue) or gained (red) chromosomes, relative to the mean expression from the genes on diploid chromosomes. The black dashed line indicates the predicted amount of mRNA from gained chromosomes in the absence of compensation. Transcriptomic data are obtained from Zerbib and colleagues (14); *P* value < 0.0001, two-tailed Mann–Whitney test. **E,** Density plots of the protein expression from diploid (blue) or gained (red) chromosomes. The black dashed line indicates the predicted amount of protein in the absence of compensation. Proteomics data are obtained from Zerbib and colleagues (14); *P* value < 0.0001, two-tailed Mann–Whitney test. **F,** Comparison of the correlation between the DNA copy number levels and the mRNA and protein expression levels (in purple and orange, respectively). Correlations values obtained from the median values of the density plots. The black dotted line represents the expected correlation in the absence of dosage compensation. The correlations are below those expected without compensation, and the correlation of the protein levels to DNA copy number is lower than that of the mRNA levels. The 30% most lowly expressed transcripts/proteins were removed from the analysis to reduce noise. **G,** Density plots of the protein expression from gained chromosomes, comparing those that are not part of CORUM protein complexes (gray) to those that are part of CORUM protein complexes (red). The black dashed line indicates the predicted protein expression in the absence of compensation. Expression values are normalized to those from the proteins encoded from diploid chromosomes; *P* value < 0.0001, two-tailed Mann–Whitney test. **H,** Comparison of the differential gene dependency scores (preranked GSEA results) between the near-diploid SS48 clone (control) and the aneuploid SS6, SS119, and SS51 clones. Plot presents enrichments for the Hallmark, KEGG, Biocarta, and Reactome gene sets. Data are obtained from Zerbib and colleagues (14). Significance threshold set at *q*-value = 0.25. Enriched pathways are color-coded. NES, normalized enrichment score.

on RNA processing and degradation. Moreover, aneuploid clones were more dependent on protein degradation *via* the proteasome (Fig. 1H), consistent with ongoing proteotoxic stress and the resultant accumulation of aberrant proteins (Fig. 1B and C). These findings were independent of the p53 status of the clones (Supplementary Fig. S1C). Together, these results suggest that cells with extra chromosomes strongly rely on the downregulation of their gene expression to compensate for their extra DNA content, both at the RNA and at the protein level.

Increased RNA Synthesis and Degradation in Trisomic Cells

To explore dosage compensation in aneuploid cells, we first assessed RNA synthesis in the RPE1 clones. We focused on the most aneuploid clones, SS51 (trisomic for chromosomes 7 and 22) and SS111 (trisomic for chromosomes 8, 9, and 18), and quantified newly synthesized RNA using ethynyl uridine (5-EU) incorporation. Indeed, nascent RNA was more abundant in highly aneuploid clones, with the highest synthesis levels found in the most aneuploid clone, SS111 (Fig. 2A and B). In line with these findings, the total levels of extracted RNA were higher in the highly aneuploid clones in comparison with pseudo-diploid clones (Fig. 2C), consistent with previous studies showing the correlation between DNA and RNA content in aneuploid cells (4, 18, 21). To assess whether increased RNA synthesis is an immediate consequence of aneuploidy, we quantified the newly synthesized RNA in parental RPE1-hTERT cells (hereinafter parental RPE1 cells) 72 hours following a pulse of reversine. Interestingly, reversine-treated RPE1 cells also increased their nascent RNA levels (Fig. 2D and E), in agreement with the results obtained in the stable aneuploid clones.

Despite increased transcription, our analysis revealed that more genes were downregulated than upregulated in the highly aneuploid clones, independently of p53 mutation status ($P < 0.001$; Supplementary Fig. S2A and S2B). As multiple pathways of RNA degradation were elevated in the aneuploid clones (Fig. 1B and C), we next investigated RNA degradation in the pseudo-diploid *versus* highly aneuploid clones. GSEA showed increased RNA catabolism in highly aneuploid cells in comparison with their pseudo-diploid counterparts (Fig. 2F). We therefore leveraged our global RNA-seq data to quantify RNA degradation in the samples using "DegNorm", an algorithm developed to quantify degraded RNA and remove its effect from RNA-seq data analyses (22). We found a significant increase in the RNA degradation index (DI; a measure for RNA degradation levels) in the highly aneuploid clones (Fig. 2G). Interestingly, degraded transcripts correlated with gene length, especially in the aneuploid clones (Supplementary Fig. S2C). GSEA of the degraded genes between the pseudo-diploid and highly aneuploid clones revealed that transcripts related to the DNA damage response and to miRNA gene silencing were less degraded in the aneuploid cells (Supplementary Fig. S2D), consistent with the activation of the DDR (14) and of the miRNA machinery in aneuploid cells (as discussed below). Importantly, there was no difference in overall transcript degradation between non-gained and gained chromosomes in the highly aneuploid clones (Supplementary Fig. S2E), suggesting that the increased degradation was not chromosome-specific. We validated the increased RNA degradation in aneuploid clones by running gel electrophoresis on the total RNA extracted from the clones and quantifying the resultant "smears" (Fig. 2H and I; Supplementary Fig. S2F and S2G). We note that RNA degradation levels were highest in the most aneuploid clone, SS111, which also exhibited the highest levels of RNA synthesis (Fig. 2A and B). To further investigate the RNA degradation rate in our system, we inhibited RNA synthesis using actinomycin D and estimated the mRNA content of several transcripts with a short half-life. RNA synthesis inhibition affected the mRNA levels of these genes more strongly in the highly aneuploid clones (Fig. 2J; Supplementary Fig. S2H), indicating a higher RNA degradation rate. Together, these findings indicate that the increased DNA content in the aneuploid clones with extra chromosomes leads to increased transcription, followed by a global increase in both RNA synthesis and RNA degradation, resulting in higher RNA turnover in these cells.

Importantly, to confirm that the pathway enrichments found in our RNA-seq data analysis were not confounded by the increased levels of RNA degradation in the aneuploid clones, we repeated all differential gene expression analyses after computationally removing the degraded transcripts. We were able to recapitulate the enrichments for DNA damage response (14), RNA metabolism, and protein degradation signatures (Supplementary Fig. S2I–S2L). Interestingly, transcripts encoding for CORUM protein complex members (23) were degraded significantly more than other transcripts (Fig. 2K), in line with the increased dosage compensation observed for these proteins (Fig. 1G).

Increased NMD Activity and Dependency in Aneuploid Cells

Next, we assessed the potential mechanisms of RNA degradation. The highly aneuploid clones, SS51 and SS111, exhibited elevated transcriptional signatures of the NMD pathway (Figs. 1B, C, and 3A; Supplementary Fig. S3A). Importantly, the NMD pathway was elevated in the aneuploid clones even when the expression of genes that reside on the gained chromosomes was removed from the analysis (Supplementary Fig. S3B), indicating that this transcriptional response is not directly due to any specific copy number gain. Thus, we compared the NMD pathway activity between the highly aneuploid and pseudo-diploid clones. First, we estimated NMD activity by calculating a transcriptional signature score of described NMD targets (24). We found a significant increase in this transcriptional score in the highly aneuploid clones (Fig. 3B), consistent with the GSEA (Fig. 3A). Next, we validated this increased activity using an NMD pathway reporter system (25), which confirmed that under standard culture conditions, highly aneuploid clones elevated their NMD pathway activity in comparison with their pseudo-diploid counterparts (Supplementary Fig. S3C).

We then turned to investigate the dependency of aneuploid cells on the NMD pathway. The NMD pathway was among the very top differential dependencies of aneuploid cells in the CRISPR screen (Fig. 1H), with many of its

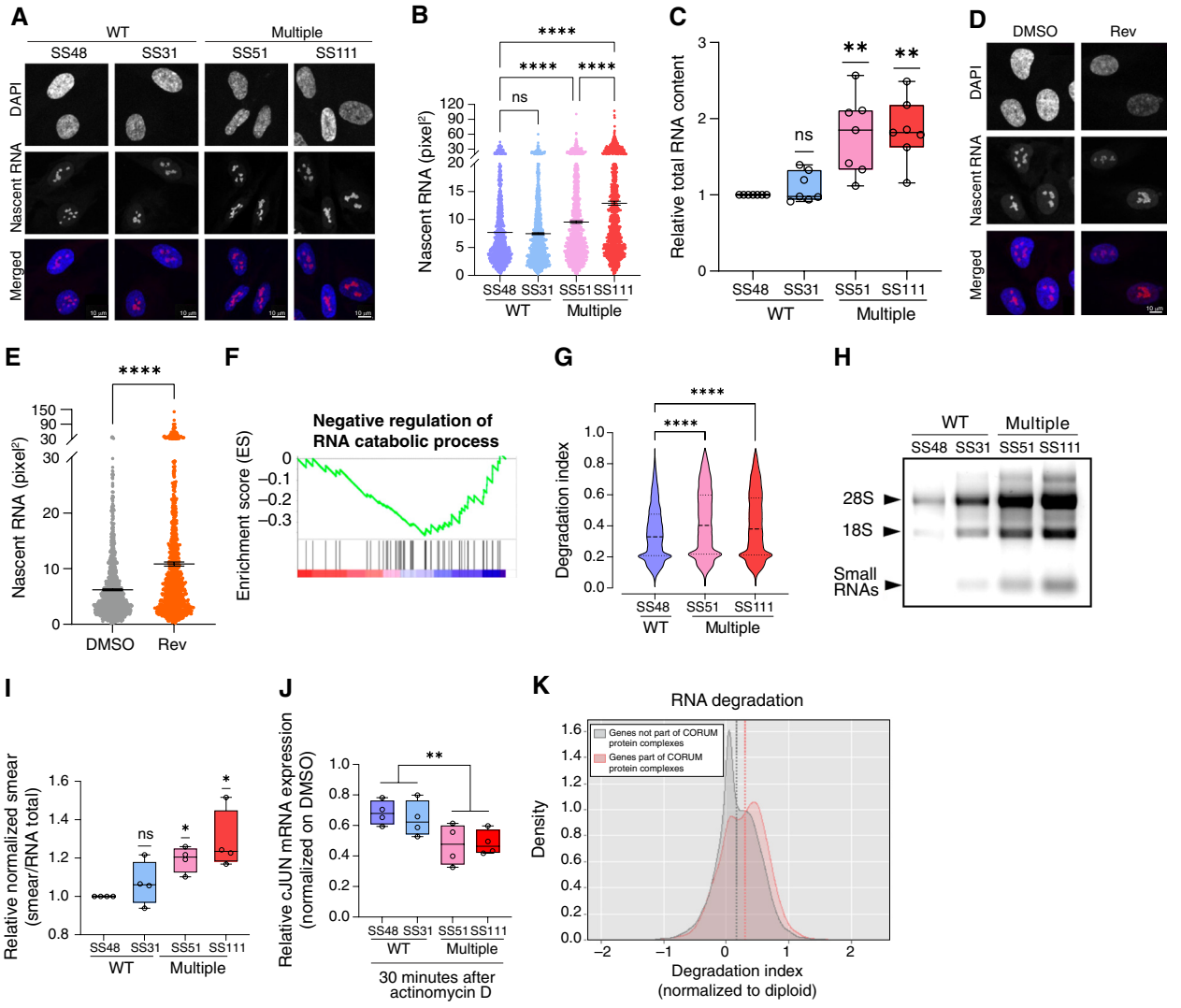

Figure 2. Trisomic cells compensate for the extra DNA content through increased RNA and protein turnover. **A,** Immunofluorescence of nascent RNA foci in pseudo-diploid clones, SS48 and SS31, and in highly aneuploid clones, SS51 and SS111. Red, nascent RNA; Blue, DAPI; Scale bar, 10 μm. **B,** Quantitative comparison of nascent RNA showing the area (pixel) of nascent RNA foci. $n = 3$ independent experiments; ****, $P < 0.0001$; Kruskal–Wallis test, Dunn multiple comparison. **C,** Quantification of total RNA between pseudo-diploid clones (SS48 and SS31) and highly aneuploid clones (SS51 and SS111). $n = 7$ independent experiments; RNA content was calculated relative to SS48, per experiment. **, $P = 0.007$ and $P = 0.0018$, for SS51 and SS111 respectively; one-sample *t* test. **D,** Immunofluorescence of nascent RNA foci in pseudo-diploid RPE1-hTERT treated with DMSO or after 72 hours following reversine pulse. Red, nascent RNA; Blue, DAPI; Scale bar, 10 μm. **E,** Quantitative comparison of nascent RNA showing the area (pixel) of nascent RNA foci. $n = 3$ independent experiments; ****, $P < 0.0001$; two-tailed Mann–Whitney test. **F,** GSEA of an RNA catabolism gene expression signature, comparing the highly aneuploid clones, SS51 and SS111, to the pseudo-diploid clone SS48. Data are obtained from Zerbib and colleagues (14). Shown is an enrichment plot for the GO-Biological Process "Negative regulation of RNA catabolic processes" gene set (NES = −1.58; *q*-value = 0.2). **G,** Comparison of the mean DI (degraded RNA score) across all genes ($n = 13{,}689$), using the DegNorm algorithm. Median DI score: 0.33 (SS48), 0.4 (SS51), and 0.38 (SS111). ****, $P < 0.0001$; repeated-measured one-way ANOVA, Tukey multiple comparison test. **H,** Native agarose gel electrophoresis of total RNA extracted from RPE1 clones, resuspended in nuclease-free water, showing a specific increased amount of RNA smear in the highly aneuploid clones, SS51 and SS111, in comparison with the pseudo-diploid clones SS48 and SS31. **I,** Quantification of RNA degradation, as evaluated by the smear/total RNA ratio. Fold change in normalized smear was calculated relative to SS48, per experiment. $n = 4$ independent experiments; *, $P = 0.0102$ and $P = 0.034$, for SS51 and SS111, respectively; one-sample *t* test. **J,** cJUN mRNA expression levels 30 minutes following actinomycin D treatment, showing increased RNA degradation rate in the highly aneuploid clones. mRNA expression was normalized to the respective vehicle-treated control. $n = 4$ independent experiments. **, $P = 0.0024$ for pseudo-diploid (SS48 and SS31) *versus* highly aneuploid clones (SS51 and SS111); two-tailed unpaired *t* test. **K,** Density plots of the RNA DI of genes that are not part of CORUM protein complexes (gray) *versus* genes that are part of CORUM protein complexes (red). Degradation values are normalized to the degradation indices of the diploid chromosomes. ****, $P < 0.0001$, two-tailed Mann–Whitney test.

components ranking among the most differentially essential genes (Fig. 3C). Importantly, these results held true even when the p53-mutated SS77 clone was included in the analysis (Supplementary Figs. S1C and S3D), indicating that the increased dependency of aneuploid cells on NMD is not simply due to p53 activation. To validate this dependency, we exposed the RPE1 clones to pharmacologic inhibitors of NMD, ouabain and digoxin (25), and found that the highly

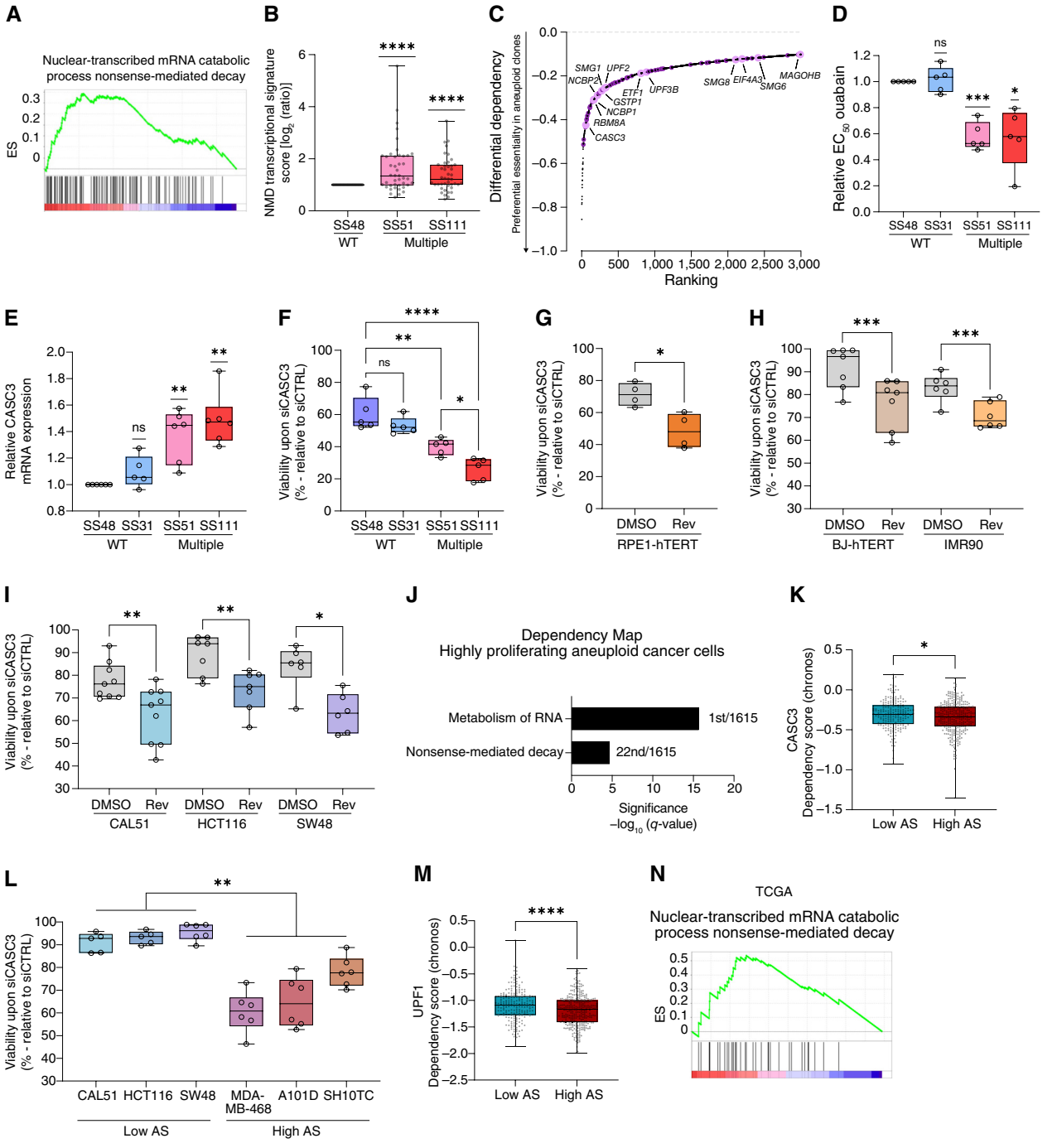

Figure 3. Aneuploid cells activate the NMD pathway and depend on this pathway for downregulating their gene expression. **A,** GSEA of an NMD-related signature, comparing the highly aneuploid clones, SS51 and SS111, to the pseudo-diploid clone SS48. Shown is the enrichment plot for the GO-Biological Process "Nuclear-transcribed mRNA catabolic processes NMD" gene set (NES = 1.83; *q*-value = 0.07). Data are taken from Zerbib and colleagues (14). **B,** Comparison of gene expression of the NMD pathway between the highly aneuploid clones SS51 and SS111, and the pseudo-diploid clone SS48. Fold change in transcriptional score was calculated relative to SS48, for each gene ($n = 43$ genes). ****, $P < 0.0001$; one-sample *t* test. Data are obtained from Zerbib and colleagues (14). **C,** The top 3,000 genes that aneuploid clones were most preferentially sensitive to their knockout in comparison with the pseudo-diploid clone SS48, based on our genome-wide CRISPR/Cas9 screen. Highlighted are genes that belong to the NMD pathway: core member genes (in pink) and ribosomal-related genes (in purple). NMD-related genes are significantly enriched within the top 3,000 gene list; ****, $P < 0.0001$; two-tailed Fisher exact test. Data are obtained from Zerbib and colleagues (14). **D,** Comparison of sensitivity (determined by EC_{50} values) to 72 hours drug treatment with the NMD inhibitor ouabain, between pseudo-diploid clones (SS48 and SS31) and highly aneuploid clones (SS51 and SS111). EC_{50} fold change was calculated relative to SS48, per experiment. $n = 5$ independent experiments; *, $P = 0.0142$ and ***, $P = 0.0009$, for SS111 and SS51, respectively; one-sample *t* test. **E,** Comparison of *CASC3* mRNA levels, quantified by qRT-PCR, between pseudo-diploid clones (SS48 and SS31) and highly aneuploid clones (SS51 and SS111). Fold change in *CASC3* expression was calculated relative to SS48, per experiment. $n = 5$ (SS31) and $n = 6$ (SS48, SS51, SS111) independent experiments; **, $P = 0.0058$ and $P = 0.0018$, for SS51 and SS111, respectively; one-sample *t* test. **F,** Comparison of cell viability (*continued on following page*)

aneuploid clones SS51 and SS111 were significantly more sensitive to both drugs (Fig. 3D; Supplementary Fig. S3E–S3G). The effect of ouabain on the cells was mostly cytostatic, as it delayed the cell cycle of the treated cells but did not increase their apoptosis (Supplementary Fig. S3H and S3I). We then investigated CASC3 (also known as MLN51, localized on chromosome 17), the top differentially essential core member of the NMD pathway, and a key regulator of NMD pathway activation (26). We found that highly aneuploid clones upregulated their CASC3 expression in comparison with their pseudo-diploid counterparts (Fig. 3E). Moreover, CASC3 protein expression levels increased following reversine-mediated aneuploidization of the parental RPE1 cells, and this increase was observed also in *TP53*-KD and *TP53*-KO RPE1 cells, indicating a p53-independent mechanism (Supplementary Fig. S3J–S3M). Aneuploid clones were significantly more sensitive to genetic CASC3 inhibition by siRNA, and the degree of the response to CASC3 depletion was associated with the degree of aneuploidy (Fig. 3F; Supplementary Fig. S3N–S3Q). In addition, reversine-induced aneuploidization of the parental pseudo-diploid RPE1 cells also rendered the cells more sensitive to CASC3 inhibition (Fig. 3G; Supplementary Fig. S4A). This effect was not limited to RPE1 cells—we induced aneuploidy using reversine in two additional near-diploid non-transformed cell lines (BJ-hTERT and IMR90) and in three additional near-diploid cancer cell lines (CAL51, HCT116, and SW48). We found that aneuploidization renders the cells sensitive to CASC3 depletion across cell lines (Fig. 3H and I; Supplementary Fig. S4B). Finally, intrigued by previous observations showing that NMD could get activated by the DDR (27, 28), we found that DNA damage induction using etoposide increased CASC3 expression levels in parental RPE1 cells (Supplementary Fig. S4C and S4D), providing a plausible mechanistic link between the increased DNA damage observed in the aneuploid cells (14) and their increased expression of, and dependency on, the NMD pathway. Together, these results confirm that aneuploidy increases cellular dependency on the NMD pathway.

Lastly, we asked whether NMD activity and dependency are linked to a high degree of aneuploidy in human cancer cells. Gene expression analysis of hundreds of human cancer cell lines revealed that RNA metabolism and particularly RNA degradation through the NMD pathway were strongly associated with the proliferation capacity of highly aneuploid cancer cell lines (but not with that of near-euploid cancer cell lines; see "Methods"; Fig. 3J). Moreover, analysis of CRISPR screens revealed that highly aneuploid cancer cells were significantly more dependent on multiple members of the NMD pathway, including CASC3 and the core NMD effector UPF1 (Fig. 3K and L; Supplementary Fig. S4E–S4H). To validate this finding in additional models, we depleted CASC3 in three representative near-diploid (CAL51, HCT116, and SW48) and three representative highly aneuploid (MDA-MB-468, A101D, and SH10TC) cancer cell lines. Indeed, highly aneuploid cancer cell lines were significantly more sensitive to CASC3 depletion (Fig. 3M; Supplementary Fig. S4I). Finally, we found a significant association between aneuploidy levels and the NMD signature across human primary tumors as well (Fig. 3N). We conclude that NMD activity and dependency are associated with a high degree of aneuploidy in cancer cells.

Increased miRNA-Mediated RNA Degradation and Altered Gene Splicing in Aneuploid Cells

The NMD pathway was not the only RNA degradation pathway that came up in our unbiased genomic and functional analyses. GSEA showed significant enrichment for signatures associated with gene expression silencing *via* small RNA pathways (Figs. 1B, C, and 4A). This enrichment was conserved when the genes expressed from the gained chromosomes were removed from the analysis (Supplementary Fig. S5A). Importantly, genome-wide miRNA profiling of our clones (14) revealed a significant overlap between downregulated mRNAs and the known targets of miRNA that were upregulated in aneuploid clones (Fig. 4B; Supplementary Fig. S5B), confirming the role of miRNAs in regulating mRNA expression in aneuploid clones. Additionally, GSEA of near-

Figure 3. ***(Continued)*** following pooled siRNA against *CASC3* for 72 hours, between pseudo-diploid clones (SS48 and SS31) and highly aneuploid clones (SS51 and SS111). Viability was calculated relative to a control siRNA treatment. $n = 5$ independent experiments; *, $P < 0.05$; **, $P < 0.01$; ****, $P < 0.0001$; One-Way ANOVA, Tukey's multiple comparison. All comparisons between SS31 and aneuploid clones were significant as well (*, $P < 0.05$). **G,** Comparison of cell viability following siRNA against *CASC3*, between parental RPE1 cells treated for 20 hours with the SAC inhibitor reversine (500 nmol/L) or with control DMSO, then harvested 72 hours post wash-out. Relative viability was calculated relative to a control siRNA treatment. $n = 4$ independent experiments; *, $P = 0.0425$; two-tailed paired *t* test. **H,** Comparison of cell viability following siRNA against *CASC3* in additional pseudo-diploid non-transformed cell lines (BJ-hTERT and IMR90), treated for 36 hours with the SAC inhibitor reversine (500 nmol/L) or with control DMSO and then harvested 72 hours post wash-out. Relative viability was calculated relative to control siRNA treatment. $n = 7$ (BJ-hTERT) and $n = 6$ (IMR90) independent experiment. ***, $P = 0.0006$ and $P = 0.0004$ for BJ-hTERT and IMR90 respectively; one-tailed paired *t* test. **I,** Comparison of cell viability following siRNA against *CASC3* in additional pseudo-diploid cancer cell lines (CAL51, HCT116, and SW48), treated for 24 hours with the SAC inhibitor reversine (125 nmol/L for CAL51 and HCT116, 200 nmol/L for SW48) or with control DMSO, then harvested 72 hours post wash-out. Relative viability was calculated relative to control siRNA treatment. $n = 9$ (CAL51), $n = 7$ (HCT116) and $n = 6$ (SW48) independent experiment. *, $P = 0.0114$ for SW48, **, $P = 0.0061$ and $P = 0.0084$ for CAL51 and HCT116 respectively; one-tailed paired *t* test. **J,** Gene set enrichment analysis of the genes in which expression correlates with proliferation in highly aneuploid cancer cell lines but not in near-diploid cancer cell lines, reveals significant enrichment of multiple RNA metabolism signatures. Shown here are the Reactome "Metabolism of RNA" and "Nonsense-mediated decay" gene sets. Significance values represent the FDR *q*-values. The ranking of each RNA metabolism signature (out of all signatures included in the gene set collection) is indicated next to each bar. **K** and **L,** Comparison of gene dependency (determined by Chronos score) for key members of the NMD pathway, the EJC member *CASC3* (**K**), and the main effector *UPF1* (**L**), between the top and bottom aneuploidy quartiles of human cancer cell lines ($n = 538$ cell lines). Data were obtained from the DepMap CRISPR screen, 22Q1 release. *, $P = 0.0289$ and ****, $P < 0.0001$, for CASC3 and UPF1 respectively; two-tailed Mann–Whitney test. **M,** Comparison of cell viability following siRNA against CASC3 in three representative pseudo-diploid cancer cell lines (CAL51, HCT116, and SW48) vs. three representative highly aneuploid cancer cell lines (MDA-MB-468, A101D, and SH10TC), harvested 72 hours post wash-out. Viability was calculated relative to control siRNA treatment. $n = 5$ (CAL51, HCT116) and $n = 6$ (SW48, MDA-MB-468, A101D, and SH10TC) independent experiment. ***, $P = 0.0049$ for lowly *versus* highly aneuploid cell lines; one-tailed unpaired *t* test, comparing the mean value of each cell line. **N,** Pre-ranked GSEA of mRNA expression levels showing that high aneuploidy levels are associated with upregulation of the NMD in human primary tumors. Shown is the GO-Biological Process "Nuclear-transcribed mRNA catabolic processes NMD" gene set (NES = 1.70, *q*-value = 0.029) gene set. Data were obtained from the TCGA mRNA expression data set (58). ES, enrichment score.

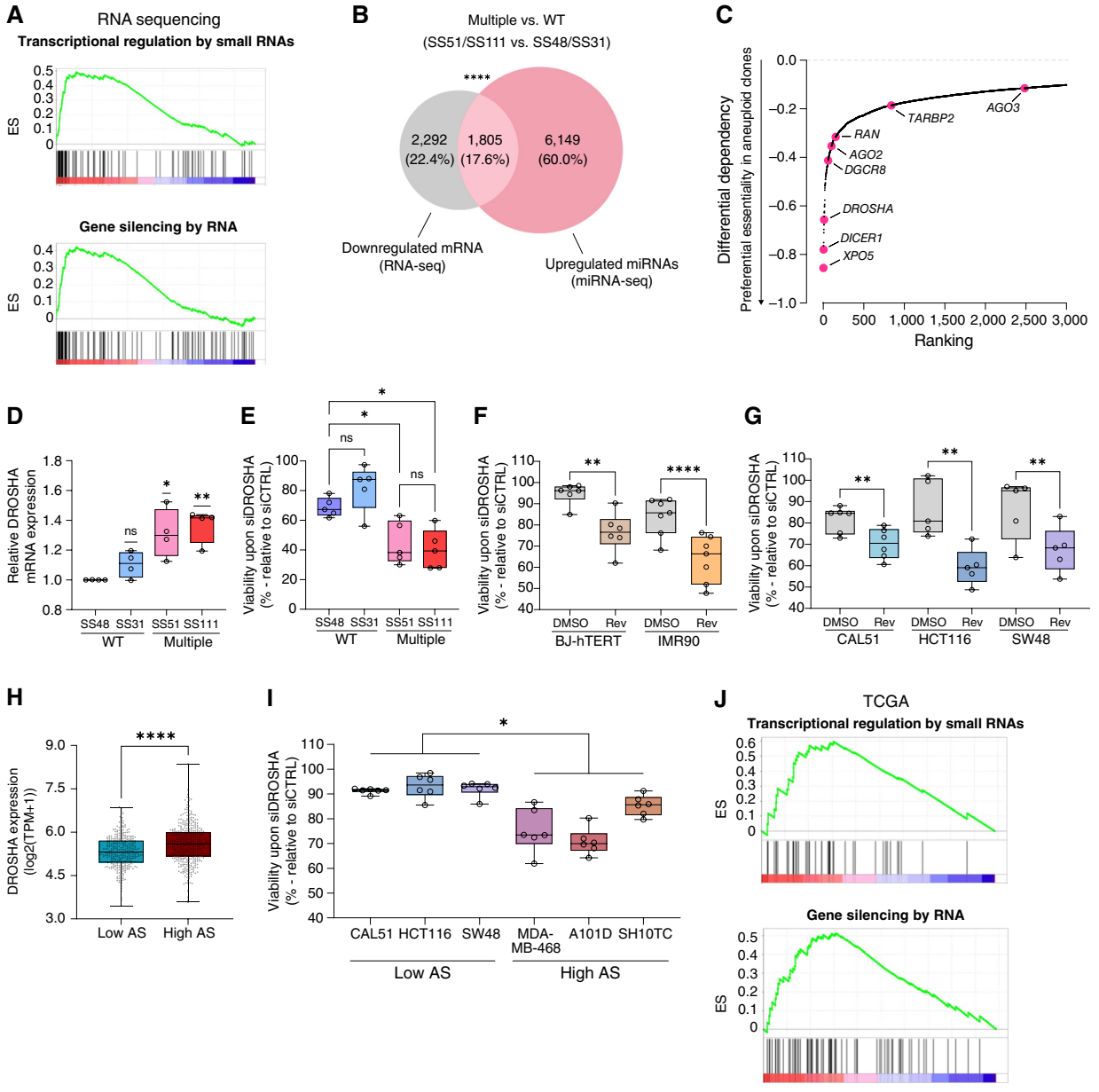

Figure 4. Aneuploid cells activate the miRNA pathway and depend on this pathway for downregulating their gene expression. **A,** GSEA of miRNA-related signatures, comparing the highly aneuploid clones, SS51 and SS111, to the pseudo-diploid clone SS48. Shown are enrichment plots for the Reactome "Transcriptional regulation by small RNAs" (NES = 2.64; *q*-value < 0.0001) and the Reactome "Gene silencing by RNA" (NES = 2.36; *q*-value = 0.00016) gene sets. Data are obtained from Zerbib and colleagues (14). **B,** Venn diagram of the overlap between downregulated mRNAs (in gray) and upregulated miRNAs (in pink) in highly aneuploid clones (SS51 and SS111) vs. pseudo-diploid clones (SS48 for the mRNA and SS48/SS31 for the miRNA). ****, $P < 0.0001$, one-sided χ^2 test. **C,** The top 3,000 genes that aneuploid clones were most preferentially sensitive to their knockout in comparison with the pseudo-diploid clone SS48, based on our genome-wide CRISPR/Cas9 screen. Highlighted are genes that belong to the miRNA biogenesis pathway (in pink), based on the Reactome "miRNA biogenesis" signature (RNA polymerase II genes excluded). miRNA genes are significantly enriched within the top 3,000 gene list. **, $P = 0.0064$; two-tailed Fisher Exact test. Data are obtained from Zerbib and colleagues (14). **D,** Comparison of DROSHA mRNA levels, quantified by qRT-PCR, between pseudo-diploid clones (SS48 and SS31) and highly aneuploid clones (SS51 and SS111). Fold change in DROSHA expression was calculated relative to SS48, per experiment. $n = 4$ independent experiments; *, $P = 0.0325$ and **, $P = 0.0079$, for SS51 and SS111, respectively; one-sample *t* test. **E,** Comparison of cell viability following siRNA against DROSHA for 72 hours, between pseudo-diploid clones (SS48 and SS31) and highly aneuploid clones (SS51 and SS111). Viability was calculated relative to control siRNA. $n = 5$ independent experiments; *, $P = 0.0425$ (SS48/SS51) and $P = 0.0148$ (SS48/SS111); One-Way ANOVA, Tukey multiple comparison test. All comparisons between SS31 and aneuploid clones were significant as well (**, $P < 0.01$). **F,** Comparison of cell viability following siRNA against DROSHA in additional pseudo-diploid non-transformed cell lines (BJ-hTERT and IMR90), treated for 36 hours with the SAC inhibitor reversine (500 nmol/L) or with control DMSO, then harvested 72 hours post wash-out. Viability was calculated relative to control siRNA treatment. $n = 6$ (BJ-hTERT) and $n = 7$ (IMR90) independent experiments. **, $P = 0.0027$ and ****, $P < 0.0001$ for BJ-hTERT and IMR90 respectively; one-tailed paired *t* test. **G,** Comparison of cell viability following siRNA against DROSHA in additional pseudo-diploid cancer cell lines (CAL51, HCT116, and SW48), treated for 24 hours with the SAC inhibitor reversine (125 nmol/L for CAL51 and HCT116, 200 nmol/L for SW48) or with control DMSO, then harvested 72 hours post wash-out. Viability was calculated relative to control siRNA treatment. $n = 6$ (CAL51), $n = 5$ (HCT116 and SW48) independent experiments. **, $P = 0.0073$; $P = 0.0024$ and $P = 0.0069$ for CAL51, HCT116 and SW48, (*continued on following page*)

diploid HCT116 cells treated with reversine also showed upregulation of miRNA pathway-related signatures (Supplementary Fig. S5C), emphasizing the generalizability of this association.

Similar to the NMD pathway, the miRNA pathway was among the top differentially essential pathways in aneuploid cells (Figs. 1H and 4C), with the hallmark miRNA pathway genes *XPO5*, *DICER1*, and *DROSHA* scoring among the 20 most differentially essential genes overall (Fig. 4C). As DROSHA (localized on chromosome 5) is the most upstream core member of this pathway, we investigated its activity and the sensitivity to its inhibition in the RPE1 clones. The highly aneuploid clones significantly increased DROSHA mRNA and protein expression (Fig. 4D; Supplementary Fig. S5D) and were significantly more sensitive to siRNA-mediated DROSHA depletion, in comparison with the pseudo-diploid clones (Fig. 4E; Supplementary Fig. S5D–S5G). Aneuploid clones with a single trisomy displayed an intermediate phenotype (Fig. 4D; Supplementary Fig. S5D–S5G). Reversine-induced aneuploidization of additional near-diploid non-transformed (BJ-hTERT and IMR90) and cancer (CAL51, HCT116, and SW48) cell lines increased their sensitivity to DROSHA depletion (Fig. 4F and G; Supplementary Fig. S5H), confirming the link between aneuploidy and DROSHA dependency.

In line with these findings, DROSHA was also significantly overexpressed in highly aneuploid human cancer cell lines compared with near-diploid ones (Fig. 4H). Comparing three near-diploid and three highly aneuploid cancer cell lines confirmed that highly aneuploid cancer cell lines were more dependent on DROSHA (Fig. 4I; Supplementary Fig. S5I). Aneuploid human cancer cell lines were more dependent on various other members of the miRNA pathway, and in particular on core members of the RNA-induced silencing complex, or RISC, such as PACT (also known as PRKRA) and TRBP (also known as TARBP2; Supplementary Fig. S6A and S6B). In line with these findings, the aneuploid RPE1 clones were preferentially more sensitive to the depletion of PRKRA and TARBP2 (Supplementary Fig. S6C–S6F), and aneuploidization increased the sensitivity to the depletion of these genes in two additional near-diploid non-transformed and three additional near-diploid cancer cell lines (Supplementary Fig. S6G–S6L). Moreover, depletion of PRKRA and TARBP2 in three near-diploid and three highly aneuploid cancer cell lines further confirmed that highly aneuploid cancer cells are more sensitive to the depletion of these RISC complex partners (Supplementary Fig. S6N–S6P). Lastly, a high degree of aneuploidy was significantly associated with elevated expression of the miRNA pathway across human primary tumors as well (Fig. 4J). Together, these results suggest that miRNA-mediated gene silencing plays an important role in regulating gene expression in aneuploid cells.

Notably, we observed that the aneuploidy-induced changes in RNA metabolism were not limited to RNA degradation—RNA splicing was also among the most differentially essential pathways in our CRISPR screens (Fig. 1H). Examining splicing activity in our model system, we observed the downregulation of several splicing signatures in highly aneuploid clones (Supplementary Fig. S6Q). Splicing analysis of RNA-seq data confirmed a significant decrease in both 5′ and 3′ alternative splicing in the aneuploid clones (Supplementary Fig. S6R–S6S). These findings align with the reported competitive interplay between miRNA biogenesis and RNA splicing (29), underscoring the miRNA pathway's significance in aneuploid clones.

We conclude that various aspects of RNA metabolism are altered in aneuploid cells with extra chromosomes and propose that these cells suffer from transcriptional burden that is offset by increased RNA degradation, making them dependent on the increased activity of two major RNA degradation mechanisms: NMD and miRNAs.

Increased Proteotoxic Stress and Reduced Translation in Aneuploid Cells

Proteotoxic stress has been reported to be associated with aneuploidy in both yeast (7–11) and engineered aneuploid mammalian cells (2, 21, 30–32), leading to reduced protein translation and increased protein degradation, which contributes to dosage compensation at the protein level. Indeed, we identified ongoing proteotoxic stress in our aneuploid clones (Fig. 1B and C; Supplementary Fig. S1A). GSEA showed that highly aneuploid clones, SS51 and SS111, upregulated gene expression signatures of proteotoxic stress and protein degradation compared with the pseudo-diploid clone SS48 (Fig. 5A). To validate these results, we characterized the UPR—the primary consequence of proteotoxic stress—in the RPE1 clones. We investigated the three main branches of the UPR (33) and detected the activation of all of them in highly aneuploid clones: increased mRNA expression of the active XBP1 and EDEM1, indicating elevated activity of the IRE1α branch (Fig. 5B); increased mRNA and protein levels of the chaperone GRP78 (also known as BiP), indicating elevated activity of the ATF6 branch (Fig. 5B–D); and increased protein levels of PERK and ATF4, as well as increased mRNA levels of CHOP, indicating elevated activity of the PERK branch (Fig. 5B–D). These findings confirm the aneuploidy-induced UPR signatures identified by our RNA-seq and proteomics data analysis (Figs. 1B, C, and 5A), in line with the need for dosage compensation at the protein level (Fig. 1E–G). Next, we functionally

Figure 4. ***(Continued)*** respectively; one-tailed paired *t* test. **H,** Comparison of DROSHA mRNA expression levels between the top and bottom aneuploidy quartiles of human cancer cell lines ($n = 738$ cell lines). Data were obtained from the DepMap Expression 22Q1 release. DROSHA mRNA expression is significantly higher in highly aneuploid cancer cell lines. ****, $P < 0.0001$; two-tailed Mann–Whitney test. **I,** Comparison of cell viability following siRNA against DROSHA in three representative pseudo-diploid cancer cell lines (CAL51, HCT116, and SW48) vs. three representative highly aneuploid cancer cell lines (MDA-MB-468, A101D, SH10TC), harvested 72 hours post wash-out. Viability was calculated relative to control siRNA treatment. $n = 6$ independent experiments. *, $P = 0.0129$ for lowly *versus* highly aneuploid cell lines; one-tailed unpaired *t* test, comparing the mean value of each cell line. **J,** Pre-ranked GSEA of mRNA expression levels showing that high aneuploidy levels are associated with upregulation of gene silencing in human primary tumors. Shown are the Reactome "Transcriptional regulation by small RNAs" (NES = 1.98; *q*-value = 0.001) and the Reactome "Gene silencing by RNA" (NES = 1.86; *q*-value = 0.004) gene sets. Data were obtained from the TCGA mRNA expression data set (58). ES, enrichment score.

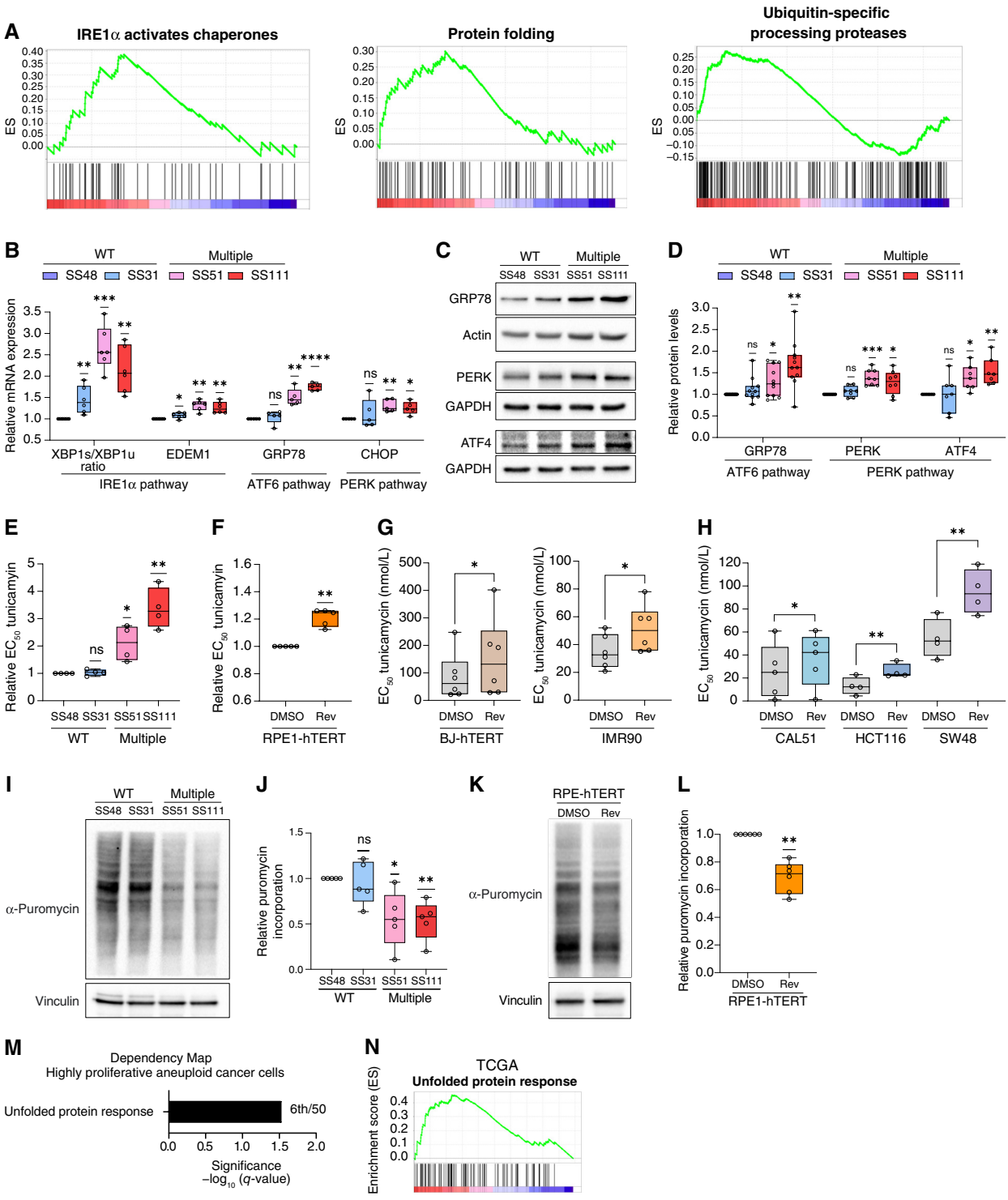

Figure 5. Aneuploid cells experience proteotoxic stress and attenuate protein translation. **A,** GSEA of proteotoxic stress-related signatures, comparing the highly aneuploid clones, SS51 and SS111, to the pseudo-diploid clone SS48. Shown are the enrichment plots for the Reactome gene sets "IRE1α activates chaperones" (NES = 1.77; *q*-value = 0.022), "Protein folding" (NES = 1.55, *q*-value = 0.084), and "Ub-specific processing proteases" (NES = 1.67, *q*-value = 0.041). Data are obtained from Zerbib and colleagues (14). **B,** Comparison of UPR mRNA levels, quantified by qRT-PCR, between pseudo-diploid (SS48 and SS31) and highly aneuploid clones (SS51 and SS111). The expression levels of the following canonical members of the UPR were measured: XBP1-spliced/XBP1-unspliced ratio and EDEM1 (IRE1α pathway), GRP78 (ATF6 pathway) and CHOP (PERK pathway). Fold change in expression was calculated relative to SS48, per experiment. $n = 6$ (XBP1 ratio, EDEM1) or $n = 5$ (GRP78, CHOP) independent experiments. XBP1 ratio: *, $P = 0.0194$; **, $P = 0.0035$ and ***, $P = 0.0005$ for SS31, SS111, and SS51, respectively EDEM1: *, $P = 0.0382$ and **, $P = 0.0015$ and $P = 0.0052$ for SS31, SS51, and SS111, respectively. GRP78: **, $P = 0.0043$ and ****, $P < 0.0001$ for SS51 and SS111, respectively. CHOP: *, $P = 0.0197$ and **, $P = 0.0095$ for SS111 and SS51, respectively; one-sample *t* test. **C,** Western blots of GRP78, PERK, and ATF4 protein levels in pseudo-diploid clones (*continued on following page*)

characterized the UPR in the cells by measuring the response of the isogenic cell lines to the endoplasmic reticulum (ER) stress inducer, tunicamycin. In line with their higher basal level of ER stress, aneuploid clones were significantly more resistant to UPR induction (Fig. 5E; Supplementary Fig. S7A and S7B). Furthermore, parental RPE1 cells became more resistant to tunicamycin following reversine exposure (Fig. 5F). We confirmed this increased resistance to ER stress induction in additional non-transformed cell lines (BJ-hTERT and IMR90), and additional near-diploid cancer cell lines (CAL51, HCT116, and SW48), in which we induced aneuploidy by MPS1 inhibition (Fig. 5G and H). Reversine-mediated aneuploidization of these models was also associated with activation of multiple UPR markers (Supplementary Fig. S7C–S7G). We then turned to another isogenic system of RPE1 cells and their aneuploid derivatives, RPTs(34). In this model, RPE1 cells have doubled their genomes following cytokinesis inhibition, resulting in chromosomal instability and highly aneuploid cells (34). RPT cells also exhibit resistance to ER stress induction using tunicamycin (Supplementary Fig. S7H). Finally, RNA-seq of near-diploid human colon cancer cells, HCT116, treated with reversine, also revealed significant enrichment for the UPR signature (Supplementary Fig. S7I), showing the importance of this process in aneuploid cells to manage the increased protein load.

UPR activation in response to the accumulation of misfolded proteins results in translation attenuation (33). To investigate whether UPR attenuates translation in our model, we performed a SUnSET puromycin incorporation assay (35). Puromycin incorporation significantly decreased in the aneuploid clones (Fig. 5I and J; Supplementary Fig. S7J and S7K), confirming that global translation levels are reduced in these cells. Importantly, reduced translation in aneuploid cells was confirmed following cell cycle synchronization, demonstrating that the decrease in translation is not merely due to a slower proliferation rate (Supplementary Fig. S7L-N). We also found that RPTs exhibited decreased levels of global translation (Supplementary Fig. S7O and S7P) and that reversine-mediated aneuploidization of the parental RPE1 cells resulted in a similar reduction in global translation (Fig. 5K and L), further demonstrating that ER stress and reduced translation are an immediate consequence of aneuploidy. Interestingly, NMD inhibition using ouabain resulted in proteotoxic stress, and its effect was significantly stronger in the aneuploid clones than in their pseudo-diploid counterparts (Supplementary Fig. S7Q and S7R), linking the compensation mechanisms at the RNA and protein levels.

Finally, gene expression analysis of hundreds of human cancer cell lines showed significant enrichment for UPR in highly proliferative highly aneuploid cancer cell lines (Fig. 5M), in line with a recent report (4). Moreover, a lineage-controlled pan-cancer analysis of The Cancer Genome Atlas (TCGA) mRNA expression datasets revealed a significant elevation of the UPR gene expression signature in highly aneuploid tumors (Fig. 5N), consistent with a recent TCGA analysis that associated UPR with copy number alterations in general (36). Therefore, we conclude that both non-transformed and cancerous aneuploid cells suffer from proteotoxic stress and must develop compensatory mechanisms to overcome it. One such mechanism is the reduction of the global translation levels, which may be partly responsible for the protein-level dosage compensation observed in aneuploid cells (3, 4, 18, 20, 21).

Increased Proteasome Activity and Dependency in Aneuploid Cells

Proteotoxic stress also leads to protein degradation through the ubiquitin-proteasome system (37). Indeed, our transcriptiomics and proteomics analyses suggested protein degradation to be elevated in the aneuploid clones (Fig. 1B

Figure 5. ***(Continued)*** (SS48 and SS31) and highly aneuploid clones (SS51 and SS111). β-Actin and GAPDH were used as housekeeping controls. **D,** Quantification of GRP78, PERK, and ATF4 protein levels, calculated relative to SS48 per experiment. GRP78 ($n = 11$ independent experiments): *, $P = 00193$ and **, $P = 0.0019$ for SS51 and SS111 respectively; PERK ($n = 8$ independent experiments): *, $P = 0.0245$ and ***, $P = 0.0005$ for SS51 and SS111, ATF4 ($n = 7$ independent experiments): *, $P = 0.0122$ and **, $P = 0.0041$ for SS51 and SS111 respectively; One-sample *t* test. **E,** Comparison of drug sensitivity (determined by EC_{50} values) to 48 hours treatment with the UPR activator tunicamycin, between pseudo-diploid clones (SS48 and SS31) and highly aneuploid clones (SS51 and SS111). EC_{50} fold change was calculated relative to SS48, per experiment. $n = 4$ independent experiments; *, $P = 0.004$ and **, $P = 0.0079$, for SS51 and SS111, respectively; one-sample *t* test. **F,** Comparison of drug sensitivity (determined by EC_{50} values) to 48 hours treatment with the UPR activator tunicamycin, between parental RPE1 cells treated for 20 hours with the SAC inhibitor reversine (500 nmol/L) or with control DMSO. $n = 5$ independent experiments. EC_{50} fold change was calculated relative to RPE1-DMSO cells, per experiment. **, $P = 0.0017$; one-sample *t* test. **G,** Comparison of drug sensitivity (determined by EC_{50} values) to 48 hours treatment with UPR activator tunicamycin, in additional non-transformed cell lines (BJ-hTERT and IMR90) treated for 36 hours with the SAC inhibitor reversine (500 nmol/L) or with control DMSO. $n = 6$ independent experiments; *, $P = 0.0223$ and $P = 0.0105$ for BJ-hTERT and IMR90, respectively, one-tailed paired *t* test. **H,** Comparison of drug sensitivity (determined by EC_{50} values) to 48 hours treatment with UPR activator tunicamycin, in additional near-diploid cancer cell lines (CAL51, HCT116, SW48) treated for 24 hours with the SAC inhibitor reversine (125 nmol/L for CAL51 and HCT116, 200 nmol/L for SW48) or with control DMSO. $n = 5$ (CAL51) or $n = 4$ (HCT116, SW48) independent experiments. *, $P = 0.0334$ and **, $P = 0.0022$ and $P = 0.0094$ for CAL51, HCT116 and SW48. respectively; one-tailed paired *t* test. **I,** Representative image of a SUnSET puromycin incorporation assay, showing a reduction in global translation in highly aneuploid clones (SS51 and SS111) in comparison with pseudo-diploid clones (SS48 and SS31). Vinculin was used as a housekeeping control. **J,** Quantitative comparison of SUnSET puromycin incorporation between pseudo-diploid (SS48 and SS31) and highly aneuploid clones (SS51 and SS111), calculated relative to SS48. $n = 5$ independent experiments; *, $P = 0.0323$ and **, $P = 0.009$ for SS51 and SS111 respectively; one-sample *t* test. **K,** Representative image of a SUnSET puromycin incorporation in parental RPE1 cells treated for 20 hours with the SAC inhibitor reversine (500 nmol/L) or with control DMSO, showing reduction in global translation following reversine-mediated aneuploidization. Vinculin was used as a housekeeping control. **L,** Quantitative comparison of SUnSET puromycin incorporation between DMSO and reversine-treated RPE1 cells, calculated relative to DMSO-treated cells. $n = 6$ independent experiments; **, $P = 0.0012$; one-sample *t* test. **M,** GSEA of the genes in which expression correlates with proliferation in highly aneuploid cancer cell lines but not in near-diploid cancer cell lines, reveals significant enrichment for UPR. Shown is the Hallmark "Unfolded Protein Response." Significance values represent the FDR *q*-values. The ranking of each proteasome signature (out of all signatures included in the gene set collection) is indicated next to each bar. Data were obtained from DepMap Expression 22Q1 release. **N,** Preranked GSEA of mRNA expression levels showing that high aneuploidy levels are associated with upregulation of the UPR in human primary tumors. Shown is the Hallmark "Unfolded Protein Response" (NES = 1.80, *q*-value = 0.001) gene set. Data were obtained from the TCGA mRNA expression data set (58). ES, enrichment score.

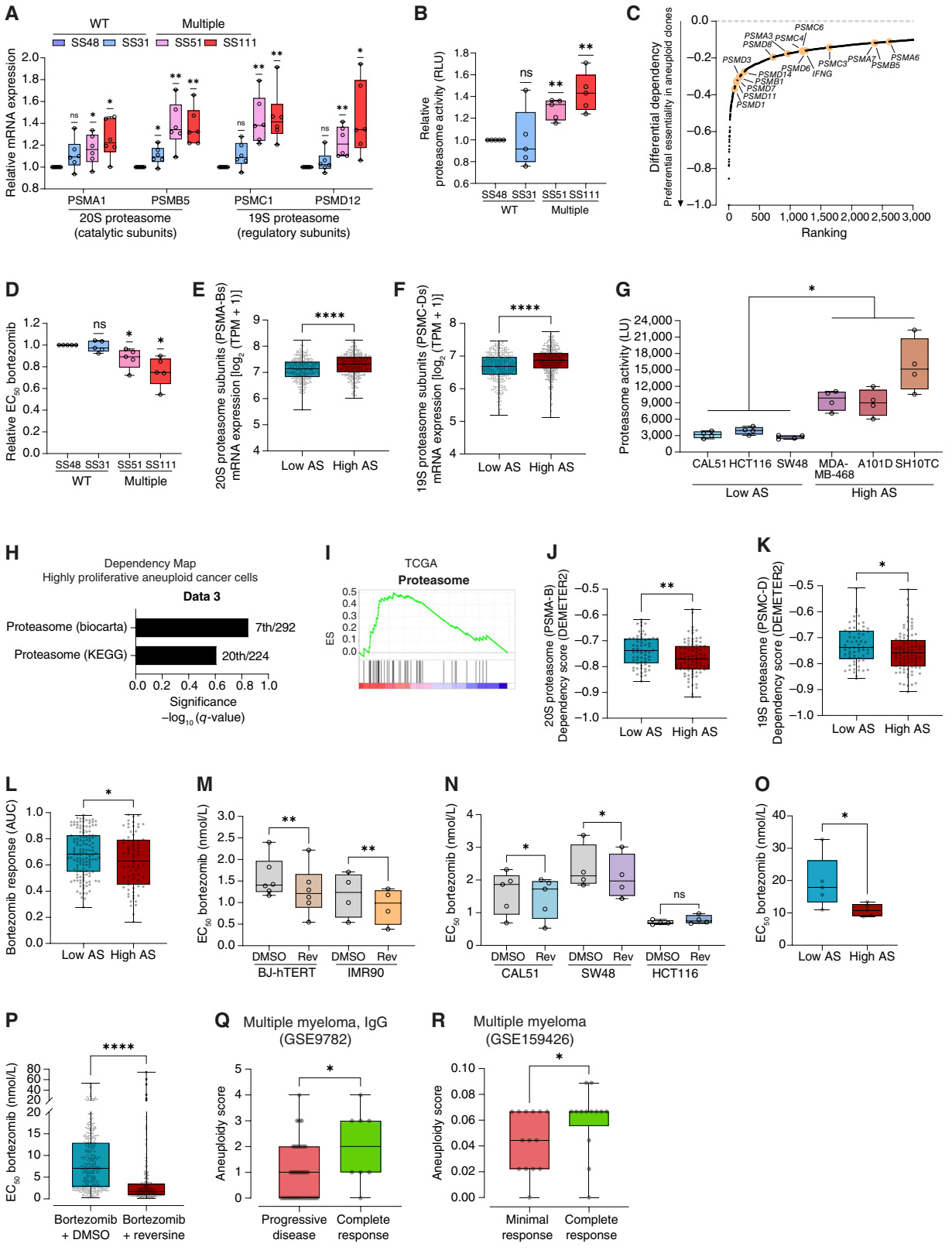

Figure 6. Aneuploid cells activate the proteasome and depend on its activity for downregulating their protein expression. **A,** Comparison of mRNA levels, quantified by qRT-PCR, between pseudo-diploid (SS48 and SS31) and highly aneuploid clones (SS51 and SS111) of representative subunits of the 20S and 19S proteasome complexes: PSMA1, PSMB5, PSMC1, PSMD12. Fold change in expression was calculated relative to SS48, per experiment. $n = 6$ independent experiments; PSMA1: *, $P = 0.0348$ and $P = 0.0155$ for SS51 and SS111 respectively, PSMB5: (*continued on following page*)

and C), and the proteasome pathway was among the top differential dependencies of aneuploid cells in the CRISPR screen (Fig. 1H). We therefore hypothesized that highly aneuploid cells increase their proteasome activity to overcome proteotoxic stress and that this makes them more vulnerable to proteasome inhibition. We validated the increased expression and activity of the proteasome complex in the RPE1 models. The highly aneuploid clones increased the expression of the proteasome subunits (Fig. 6A), suggesting an increased proteasome activity in this model. Consistent with this finding, the mRNA expression of the same proteasomal subunits was upregulated in RPT cells (Supplementary Fig. S8A), and following reversine treatment of the parental RPE1 cells (Supplementary Fig. S8B). Moreover, GSEA of reversine-treated HCT116 cells revealed that aneuploid HCT116 cells tend to increase (albeit not significantly) their proteasome expression (Supplementary Fig. S8C). We confirmed that the highly aneuploid cells significantly upregulated the chymotrypsin-like activity of their proteasome using the ProteasomeGlo assay, in the highly aneuploid RPE1 clones (Fig. 6B), in the RPT cells (Supplementary Fig. S8D), and in the parental RPE1 cells following reversine-induced aneuploidization (Supplementary Fig. S8E). Interestingly, the increase in proteasome activity corresponded well with the degree of overexpression of the proteasome subunits across all three model systems. Together, these results suggest that aneuploid cells activate the proteasome system to increase their protein degradation.

We then turned to investigate the dependency of aneuploid cells on the proteasome. Core proteasomal subunits were among the top differentially essential genes in the CRISPR screen (Fig. 6C), so aneuploid clones were significantly more sensitive to the perturbation of the 26S proteasome subunits than the pseudo-diploid clone (Supplementary Fig. S8F). To validate this finding, we exposed the RPE1 clones to two proteasome inhibitors, bortezomib (a clinically approved drug) and MG132. The highly aneuploid clones were significantly more sensitive to proteasome inhibition than their pseudo-diploid counterparts (Fig. 6D; Supplementary Fig. S8G–S8I). Bortezomib treatment induced apoptosis and the proportion of apoptotic cells following treatment was much higher in the highly aneuploid clones (Supplementary Fig. S8J). Interestingly, the most aneuploid clone, SS111, exhibited the strongest resistance to ER stress induction (Fig. 5E), the strongest proteasome subunit expression and activity (Fig. 6A and B), and the strongest sensitivity to proteasome inhibitors (Fig. 6D; Supplementary Fig. S8I and S8J), further supporting the association between aneuploidy and these cellular responses.

Next, we asked whether proteasome activity and dependency are associated with a high degree of aneuploidy in human cancer cells as well. Gene expression analysis of hundreds

Figure 6. ***(Continued)*** *, $P = 0.02789$; **, $P = 0.0064$ and $P = 0.0032$ for SS31, SS51 and SS111 respectively, PSMC1: **, $P = 0.0045$ and $P = 0.0057$ for SS51 and SS111 respectively, PSMD12: *, $P = 0.0233$ and **, $P = 0.0094$ for SS111 and SS51 respectively; one-sample *t* test. **B,** The levels of proteasome activity, measured by Proteasome-Glo, in pseudo-diploid (SS48 and SS31) and highly aneuploid clones (SS51 and SS111), showing increased proteasome activity in highly aneuploid clones. Proteasome activity was calculated relative to SS48, per experiment. $n = 5$ independent experiment, **, $P = 0.0027$ and $P = 0.0056$, for SS51 and SS111 respectively; one-sample *t* test. **C,** The top 3,000 genes that aneuploid clones were most preferentially sensitive to their knockout in comparison with the pseudo-diploid clone SS48, based on our genome-wide CRISPR/Cas9 screen. Data are obtained from Zerbib and colleagues (14). Highlighted are genes that belong to the proteasome complex (based on the KEGG "Proteasome" gene set). Proteasome genes are significantly enriched within the top 3,000 gene list; *, $P = 0.0233$; two-tailed Fisher Exact test. **D,** Comparison of drug sensitivity (determined by EC_{50} values) to 72 hours of drug treatment with the proteasome inhibitor bortezomib, between pseudo-diploid clones (SS48 and SS31) and highly aneuploid clones (SS51 and SS111). EC_{50} fold change was calculated relative to SS48, per experiment. $n = 5$ independent experiments; *, $P = 0.0437$ and $P = 0.0163$, for SS51 and SS111, respectively; one-sample *t* test. **E** and **F,** Comparison of mRNA expression levels of 20S (**E**) and 19S (**F**) proteasome subunits between the top and bottom aneuploidy quartiles of human cancer cell lines ($n = 738$ cell lines). Data were obtained from the DepMap CRISPR screen 22Q1 release. 20S and 19S mRNA expression levels are significantly increased in highly aneuploid cancer cell lines. ****, $P < 0.0001$; two-tailed Mann–Whitney test. **G,** The levels of proteasome activity, measured by ProteasomeGlo in three pseudo-diploid (CAL51, HCT116, and SW48) and three highly aneuploid (MDA-MB-468, A101D, and SH10TC) cancer cell lines. $n = 4$ independent experiments; *, $P = 0.011$ for low vs. highly aneuploid cancer cells (comparison of averaged activity for each cell line); one-tailed unpaired *t* test. **H,** GSEA of the genes in which expression correlates with proliferation in highly aneuploid cancer cell lines but not in near-diploid cancer cell lines, reveals significant enrichment of proteasome-related signatures. Shown here are the Biocarta "Proteasome" and the KEGG "Proteasome" signatures. Significance values represent the FDR *q*-values. The ranking of each proteasome signature (out of all signatures included in the gene set collection) is indicated next to each bar. Data were obtained from DepMap Expression 22Q1 release. **I,** Preranked GSEA of mRNA expression levels showing that high aneuploidy levels are associated with upregulation of the proteasome in human primary tumors. Shown is the enrichment plot of the KEGG "Proteasome" (NES = 1.65; *q*-value = 0.042) gene set. Data were obtained from TCGA mRNA expression (58). **J** and **K,** Comparison of gene dependency (determined by DEMETER2 score) for the 20S (**J**) and 19S (**K**) proteasome subunits, between the top and bottom aneuploidy quartiles of human cancer cell lines ($n = 738$ cell lines). Data were obtained from the DepMap RNAi screen, 22Q1 release. **, $P = 0.0089$ and *, $P = 0.0462$ for 20S and 19S proteasome subunits, respectively; two-tailed Mann–Whitney test. **L,** Comparison of drug sensitivity (determined by AUC) to the proteasome inhibitor bortezomib, between the top and bottom aneuploidy quartiles of human cancer cell lines ($n = 203$ cell lines). Data were obtained from GDSC1 drug screen, DepMap portal 22Q1 release. *, $P = 0.0404$; two-tailed *t* test. **M,** Comparison of drug sensitivity (determined by EC_{50} values) after 72 hours of treatment with the proteasome inhibitor bortezomib, in additional non-transformed cell lines (BJ-hTERT and IMR90) treated for 36 hours with the SAC inhibitor reversine (500 nmol/L) or with control DMSO. $n = 6$ (BJ-hTERT) and $n = 4$ (IMR90) independent experiments; **, $P = 0.0046$ and $P = 0.0078$ for BJ-hTERT and IMR90 respectively, one-tailed paired *t* test. **N,** Comparison of drug sensitivity (determined by EC_{50} values) to 72 hours treatment with the proteasome inhibitor bortezomib, in additional pseudo-diploid cancer cell lines (CAL51, HCT116, SW48) treated for 24 hours with the SAC inhibitor reversine (125 nmol/L for CAL51 and HCT116, 200 nmol/L for SW48) or with control DMSO. $n = 5$ (CAL51) or $n = 4$ (HCT116 and SW48) independent experiments. *, $P = 0.0122$ and $P = 0.0179$ for CAL51 and SW48, respectively; one-tailed paired *t* test. **O,** Comparison of drug sensitivity (determined by EC_{50} values) of 5 near-euploid (CAL51, EN, MHHNB11, SW48, and VMCUB1) and 5 highly aneuploid (MDA-MB-468, NCIH1693, PANC0813, SH10TC, and A101D) cancer cell lines to 72 hours drug treatment with the proteasome inhibitor bortezomib. *, $P = 0.0317$; Mann–Whitney test. **P,** PRISM-based (39) comparison of drug sensitivity (determined by EC_{50} values) to 120 hours treatment with the proteasome inhibitor bortezomib, between cancer cells treated with the SAC inhibitor reversine (250 nmol/L) or with control DMSO ($n = 387$ cell lines). Aneuploidy induction sensitized cancer cells to bortezomib. ****, $P < 0.0001$; two-tailed Wilcoxon rank sum test. **Q,** Comparison of the ASs of patients with multiple myeloma (IgG subtype) treated with bortezomib in monotherapy (42). Patients with a Complete Response ("responders"; $n = 8$) have significantly higher AS in comparison with patients with a progressive disease ("non-responders"; $n = 50$); *, $P = 0.014$, one-tailed Mann–Whitney test. **R,** Comparison of the ASs of patients with multiple myeloma treated with bortezomib in combination with chemotherapies and dexamethasone (43). Patients with a "Complete Response" ($n = 13$) have significantly higher AS in comparison with patients with a "Minimal Response" ($n = 14$). *, $P = 0.0382$, one-tailed Mann–Whitney test. ES, enrichment score.

of human cancer cell lines revealed increased gene expression of both the 20S and 19S proteasome subunits in highly aneuploid cancer cells (Fig. 6E and F). We assessed the activity of the proteasome by comparing chymotrypsin-like activity in three cell lines with a low degree of aneuploidy and three cell lines with a high degree of aneuploidy and found higher proteasome activity in the aneuploid cell lines (Fig. 6G). Moreover, genes associated with the proliferation capacity of highly aneuploid, but not of near-euploid, cancer cell lines were strongly enriched for proteasome signatures (Fig. 6H). Importantly, we found a significant association between aneuploidy and the proteasome gene expression signature in the TCGA dataset as well (Fig. 6I), suggesting that this association holds true in primary tumors. Together, these results suggest an increased proteasome activity in highly aneuploid cancer cells.

We then investigated the association between aneuploidy and proteasome dependency in human cancer cells. Highly aneuploid cancer cells were more dependent on genetic (shRNA-mediated) silencing of both the 20S and 19S proteasome subunits (Fig. 6J and K) and more sensitive to its pharmacologic inhibition using bortezomib (Fig. 6L). Reversine-induced aneuploidization of two near-diploid non-transformed cell lines (BJ-hTERT and IMR90) and three near-diploid cancer cell lines (CAL51, SW48 and HCT116) rendered four of the five cell lines more sensitive to bortezomib (Fig. 6M and N; note that the fifth cell line, HCT116, was extremely sensitive to the drug to begin with). Next, we selected five representative cancer cell lines with a low degree of aneuploidy and five representative cancer cell lines with a high degree of aneuploidy (38), and compared their response to bortezomib. Indeed, highly aneuploid cancer cells were more sensitive to the proteasome inhibitor (Fig. 6O; Supplementary Fig. S8K–S8M). To confirm that proteasome dependency is indeed causally related to aneuploidy in cancer cells, we assessed the response of 578 human cancer cell lines to bortezomib, using the PRISM barcoded cell line platform (39). The response to bortezomib was evaluated either in the absence or in the presence of a low dose (250 nmol/L) of reversine (see "Methods"). At this concentration, reversine had a mild effect on proliferation (Supplementary Table S4), but significantly sensitized cancer cells to proteasome inhibition (Fig. 6P). Therefore, we conclude that aneuploid cancer cells upregulate their proteasome activity in response to proteotoxic stress, rendering them more sensitive to proteasome inhibition.

Finally, we assessed whether the degree of aneuploidy could indeed predict patients' response to the FDA-approved drug bortezomib. We used gene expression data to infer the aneuploidy landscapes (40, 41) of patients with multiple myeloma treated with bortezomib as a single agent (42), or in combination with chemotherapies and with dexamethasone (43, 44). Used as a single agent, we found that within the immunoglobulin G myeloma subtype, the largest group in the dataset, the degree of aneuploidy was significantly higher in patients who exhibited complete response ($n = 8$) in comparison with patients who experienced progressive disease ($n = 50$; Fig. 6Q). Used in combination with other drugs (43), the degree of aneuploidy was also significantly higher in patients that exhibited complete response ($n = 13$) in comparison with patients who experienced progressive disease ($n = 14$; Fig. 6R). This trend was conserved in a third clinical dataset (44), in which patients with multiple myeloma were treated with bortezomib in combination with thalidomide and dexamethasone (Supplementary Fig. S8N), albeit with borderline significance due to the very low sample size of the "non-responders" group ($n = 2$). Finally, we analyzed the response to proteasome inhibitors in pancreatic and pediatric patient-derived tumor xenograft (PDX) datasets. Response of metastatic pancreatic cancer PDXs (45) to multiple proteasome inhibitors significantly correlated with their aneuploidy score (AS; Supplementary Fig. S8O–S8Q). In addition, a linear regression analysis showed a significant association between AS and response to bortezomib in a panel of pediatric PDXs (ref. 46; Supplementary Fig. S8R). Together, these analyses suggest that the degree of aneuploidy is clinically important for predicting the response of patients with cancer to bortezomib (and, presumably, to other proteasome inhibitors).

DISCUSSION

RNA Metabolism in Aneuploid Cells

Changes in gene copy number generally trigger corresponding changes in the amount of produced mRNA (7–9, 11, 16, 21, 47, 48). Accordingly, our data show that cells with gained chromosomes experience increased RNA synthesis (Fig. 2). Importantly, we also found that trisomic cells upregulate pathways involved in RNA degradation and gene silencing, and in particular the NMD and the miRNA pathways (Figs. 3 and 4). Buffering mechanisms might therefore attenuate the burden of an imbalanced karyotype. Although protein dosage compensation has been reported to occur in aneuploid cells—in both non-transformed (7–10, 16, 21, 48, 49) and cancer cells (4, 5)—the role and impact of RNA metabolism in dosage compensation is just emerging (19). Interestingly, dosage compensation at the mRNA level seems to be minimal in yeast (12, 18) but has been recently observed in human cells (4, 6).

Intriguingly, the effect of extra chromosomes on RNA metabolism is not limited to the RNA transcribed from the gained chromosomes and is enriched for genes that encode protein complex members. In line with recent reports (5, 6), we indeed found stronger dosage compensation at the protein level, which was significantly enriched for protein complex members. How aneuploid cells evolve to alter their global RNA metabolism in response to changes in gene dosage remains to be fully understood. There are at least two possible scenarios: gene silencing might be the direct consequence of increased gene expression, somehow sensed by the cells; or could be induced indirectly following aneuploidy-induced cellular stresses. We favor the latter possibility and speculate that DNA damage is a major aneuploidy-induced stress playing a role in this process. Indeed, the expression of the NMD core component CASC3 increased following DNA damage in pseudo-diploid RPE1 cells, consistent with previous reports of DDR-induced NMD activity (27, 28). We propose that aneuploidy-induced cellular stresses result in altered RNA metabolism in aneuploid cells, counteracting changes in gene expression caused by imbalanced karyotypes.

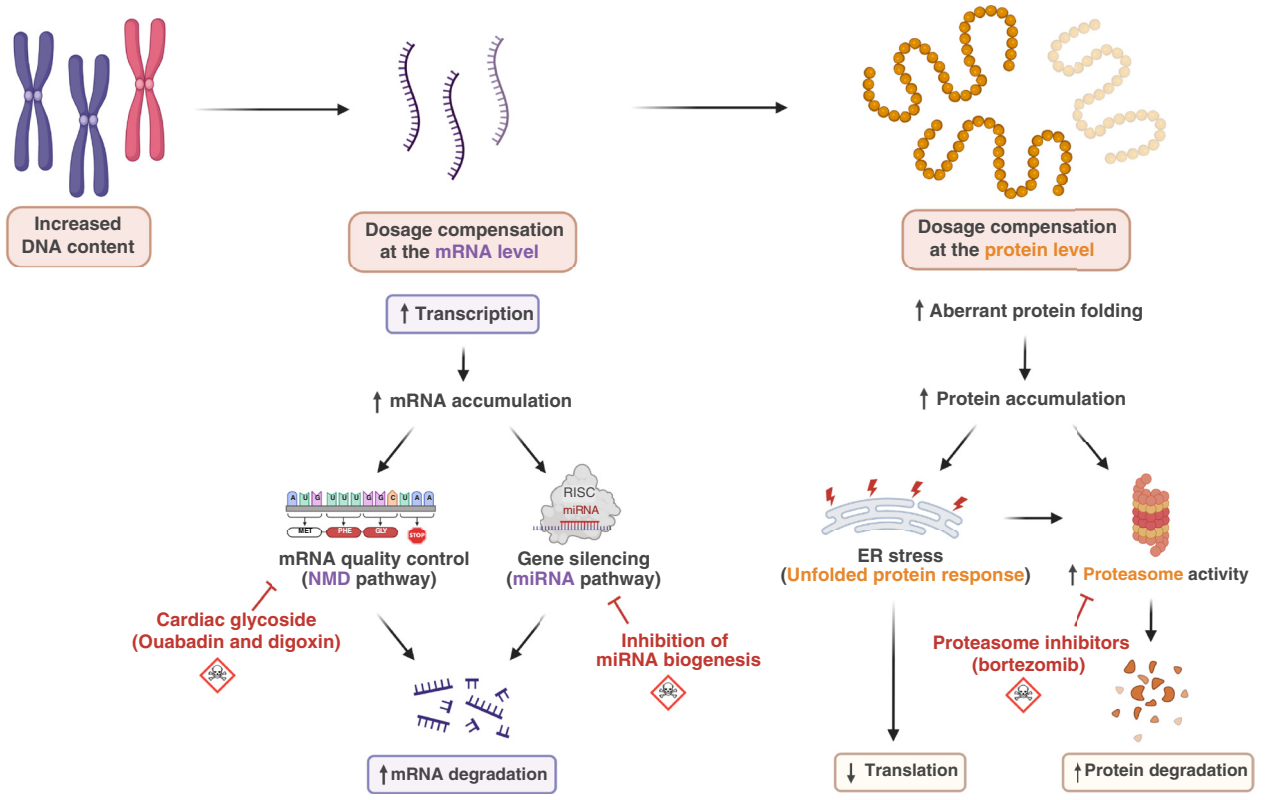

Figure 7. Aneuploid cells with extra chromosomes compensate for their excessive DNA content at both the RNA and the protein level. A summary illustration of the study. Increased DNA content leads to increased transcription in aneuploid cells, which is counterbalanced by reducing the cellular mRNA levels via activation of the NMD and the miRNA pathways. The increase in the number of total and aberrant transcripts induces accumulation of misfolded proteins that trigger the UPR. Consequently, aneuploid cells decrease their protein translation and increase their protein degradation by activating the proteasome machinery. Aneuploid cells therefore become preferentially sensitive to the perturbation of both RNA and protein metabolism.

Importantly, the increased dependency of aneuploid cells on RNA degradation was independent of p53 status (Supplementary Figs. S1 and S2), indicating that this is a consequence of the aneuploid state *per se*. We note, however, that our isogenic cell lines harbored extra chromosomes (trisomies), and the dosage compensation mechanisms that we identify are therefore associated with trisomies rather than with aneuploidy in general; different mechanisms for dosage compensation may be triggered upon monosomy (4, 50) and should be specifically addressed in future studies.

Proteotoxic Stress and Proteasome Dependency in Aneuploid Cells

Tight control of pathways involved in protein translation and degradation is crucial to limit proteotoxic stress in aneuploid cells (2, 7–9, 16, 21, 48, 49). Proteotoxic stress is perhaps the most prominent consequence of karyotype imbalances; the simultaneous overexpression of hundreds of genes on gained chromosomes results in a massive burden on protein homeostasis. The effects of aneuploidy-induced proteotoxic stress described so far are mainly as follows: (i) overwhelming of the protein-folding machinery (2, 30) and (ii) saturation of catabolic pathways responsible for the degradation of excessive proteins (9, 16, 21, 30). Importantly, our results indicate that aneuploid cells are sensing and responding to the altered demand for the synthesis, folding, and assembly of proteins both by attenuating global protein translation and by increasing global protein degradation (Fig. 5), thereby "buffering" the stoichiometric imbalance induced by aneuploidy.

Interestingly, protein buffering was recently reported to be common in cancer cells, suggesting that maintenance of proper protein complex stoichiometries is crucial for tumor growth (28). A recent TCGA analysis revealed that the abundance of proteasome subunits was correlated with the degree of stoichiometric imbalance. Here, we took this notion further, demonstrating that aneuploid cancer cells not only activate the proteasome but consequently become more dependent on its activity (Fig. 6). We show that this association holds true in data from PDXs and from human patients, and propose that aneuploidy might be a biomarker for predicting tumor's response to proteasome inhibitors.

The Advantages and Limitations of Our Datasets

The combined analyses of mRNA, miRNA, and protein expression data provide a comprehensive framework for detailed analyses of dosage compensation in isogenic aneuploid RPE1 cells. Despite high concordance among datasets, the statistical significance of proteomics data is lower than that of mRNA data, most likely due to inherently higher technical variability in proteomics analyses. Furthermore, even within

each dataset, not all genes/proteins within a given pathway behave exactly the same. This is expected, both due to the large-scale nature of these experiments, and due to biological differences across genes/proteins (e.g., when a biological pathway is downregulated, some genes in the pathway may be overexpressed because of a feedback loop and compensatory mechanisms). For these reasons, we focused our analyses of the profiling and screening data at the *pathway level*, using GSEA, and validated each pathway by targeting multiple genes using multiple targeting approaches (e.g., multiple siRNAs to knockdown a given gene, in order to reduce the off-target risk that is inherent to this type of perturbation). Importantly, at the pathway level, the proteomic data analysis recapitulated very well all of the key findings of the mRNA data analyses. Future integrative analyses of these datasets are therefore expected to yield further insights into dosage compensation in aneuploid human cells.

Concluding Remarks

Extensive transcriptome and proteome imbalance is one of the most immediate and important consequences of aneuploidy. Our work indicates that RNA and protein metabolism—and in particular their degradation—play a central role in attenuating the cellular impact of the increased DNA content that inevitably characterizes trisomic cells. Therefore, dosage compensation might be achieved by perturbation of various stages along the gene expression process (Fig. 7). Importantly, each of these stages presents a potential opportunity for therapeutic intervention: Cardiac glycosides might represent a novel class of anti-aneuploid cancer therapeutics through targeting of NMD, and proteasome inhibitors might be preferentially effective against aneuploid cancer cells because of their increased reliance on the proteasome activity (Fig. 7). Those vulnerabilities might be further exacerbated by the ongoing CIN that characterizes aneuploid cancer cells. As these drugs are already used in the clinic, clinical trials are now necessary to determine if they can indeed be used to treat aneuploid tumors.

METHODS

Cell Culture

RPE1-hTERT cells, their derivatives clones, and RPT, CAL51, HCT116, SW48, EN, VMCUB, MDA-MB-468, and A101D cell lines were cultured in DMEM (Life Technologies) with 10% FBS (Sigma-Aldrich), 1% sodium pyruvate, 4 mmol/L glutamine, and 1% penicillin–streptomycin. BJ-hTERT was cultured in DMEM supplemented with 10% FBS, 4 mmol/L glutamine, 1% sodium pyruvate, 0.01 mg/mL hygromycin (Life Technologies), and 1% penicillin–streptomycin. IMR90 was cultured in EMEM (ATCC) supplemented with 10% FBS, and 1% penicillin–streptomycin. SH10TC, NCIH1693, MHHNB11, and PANC0813 were cultured in RPMI-1640 (Life Technologies) with 10% FBS (Sigma-Aldrich) and 1% penicillin–streptomycin–glutamine (Life Technologies). PANC0813 medium was supplemented with 10 unit/mL human recombinant insulin (Sigma-Aldrich), and MHHNB11 medium was supplemented with MEM Non-Essential Amino Acids (Sigma-Aldrich). Cells were cultured at 37°C with 5% CO_2 and were maintained in culture for a maximum of 3 weeks. All cell lines were tested free of *Mycoplasma* contamination routinely using Myco Alert (Lonza) according to the manufacturer's protocol. All cell lines were kept in culture for no more than 10 passages. Cell identification details are available in Supplementary Table S5.

The detailed generation and characterization of our isogenic aneuploid clones are described in our companion study (14). Briefly, cells were seeded and synchronized with 5 mmol/L thymidine for 24 hours, then treated with 500-nmol/L reversine (or vehicle control) for 16 hours, and then sorted, propagated, and karyotyped. Aneuploid RPE1 clones proliferate a bit slower than pseudo-diploid counterparts but retain a similar mitotic timing and a similar mitotic error rate.

To synchronize the RPE1 cells for protein translation assay, cells were seeded and treated with RO-3306 for 18 hours. Cells were released by 3-time PBS washes and then harvested 6 hours post-release.

To induce random aneuploidy, RPE1 cells were seeded and synchronized with 5-mmol/L thymidine for 24 hours and then treated with 500 nmol/L reversine (or vehicle control) for 16 hours, BJ-hTERT and IMR90 were treated with 500 nmol/L reversine for 36 hours, CAL51 and HCT116 were treated with 125 nmol/L reversine for 24 hours, and SW48 was treated with 200 nmol/L reversine for 24 hours. Drug and siRNA read-outs were performed 72 hours post reversine wash-out. UPR markers estimation was performed 24 hours post reversine wash-out. For RNA-seq following reversine induction in the HCT116 cell line, cells were treated with 150 nmol/L reversine for 72 hours before harvesting.

RNA Synthesis

Cells were seeded on coverslips coated with 5 μg/mL fibronectin. Seventy-two hours later, the EZClick RNA label was incubated for 1 hour at 37°C. Then, *de novo* synthesized RNA and 4′,6-diamidino-2-phenylindole (DAPI) were detected following the manufacturer's instructions. Coverslips were mounted using Mowiol. Cells were imaged using Leica SP8 confocal microscope with a magnification objective of 40×. FIJI software was used for the quantification of nascent RNA spots area.

RNA-seq and Data Analysis

RNA sequence reads of RPE1 clones were obtained from Zerbib and colleagues (14) and were analyzed as previously described in Zerbib and colleagues (14). Normalized read counts and differential gene expression analysis were generated using the DESeq2 R package (51). GSEA and pre-ranked GSEA were performed on the differentially expressed genes using GSEA software 4.0.3, with the following parameters: 1,000 permutations and collapse analysis, using the Hallmark, KEGG, Biocarta, and Reactome gene sets (in separate analyses). Genes with fewer than 10 and 20 normalized read counts, for GSEA and pre-ranked GSEA, respectively, were excluded from further analyses.

GSEA was then performed on the modified gene expression matrix, as previously described. To control for the copy number gains in the different RPE1 clones, genes localized on the gained chromosomes were removed and the analysis was repeated.

Evaluation of degraded RNA was performed using "DegNorm" with default parameters, as previously described (22), to generate the DI and the degradation-free expression matrix. GSEA was then repeated with the degradation-free expression matrix. Gene length was obtained from the Ensembl BioMart database and correlated to the DI. Pathway enrichment analysis of the 1% of genes that were most differentially degraded between the pseudo-diploid and highly aneuploid clones was performed using MSigDB.

NMD pathway transcriptional activity was evaluated as previously described (24). Briefly, we calculated the R_{mRNA} score, i.e., the mRNA abundance of an NMD target gene, following the equation: $R_{mRNA} = mE_{NMD}/median\_mE_{non\text{-}NMD}$ (mE_{NMD} being the mRNA expression of the NMD target and $median\_mE_{non\text{-}NMD}$ being the median of mRNA

expression of non-NMD target genes). To infer the NMD pathway activity in aneuploid clones, an NMD transcriptional score, representing the relative abundance of the NMD target gene in aneuploid clones compared with pseudo-diploid RPE1-SS48, was calculated following the equation: NMD score = R_{mRNA}(aneuploid)/R_{mRNA}(SS48).

Differential splicing analysis was performed using VAST-Tool (52). RNA-seq reads were aligned against the VASTDB of the human reference genome hg19. The percent spliced-in score for each splicing event, representing the percentage of included splicing events out of total splicing events (higher the index, lower the splicing activity), was calculated using the VAST-Tool package and "compare" method, between SS48 and each one of the aneuploid samples. Biological replicates were combined to enhance read coverage and mitigate biased representation in alternative splicing events for highly expressed genes. For the downstream analysis, only the alternative 3′/5′ splice site events (Alt3 and Alt5) with a percent spliced-in score of >5 were considered.

For RNA-seq of HCT116 cells, RNA was extracted from reversine-treated cells and from DMSO control cells, and RNA quality was assessed using Tapestation. RNA library was prepared using TruSeq Stranded Total RNA kit (Illumina) following manufacturer's protocol and sequenced on Novaseq 6000 sequencer (Illumina) following manufacturer's protocol. RNA sequence reads were aligned to the human reference genome hg38 using STAR. Normalized counts and differential expression matrix of HCT116 following reversine treatment were obtained using the "DESeq2" R package. GSEA was performed on the normalized expression matrix, as described above.

Proteomics

Proteomics was obtained and performed as previously described (16). Briefly, samples were prepared from 1,000 cells, incubated for 5 minutes at 95°C while shaking, and digested at 37°C for 17 hours. Liquid chromatography–mass spectrometry followed by data-independent acquisition (DIA) was performed on an Evosep One system coupled to a Bruker timsTOF Pro 2 mass spectrometer, running DIA-PASEF. Raw data were processed using DIA-NN 1.8.1 (ref. 53; https://github.com/vdemichev/DiaNN). Human reference proteome from UniProt (54) was used for peptide and protein annotation (UP00000564, downloaded 20230327). Raw data are available on the PRIDE database under accession number PXD048833; the output table is available in Zerbib and colleagues (14). GSEA was performed as described in the RNA-seq section.

Dosage Compensation and Protein Complex Analyses

mRNA expression and protein abundance of each gene were normalized to the average expression of genes residing on the diploid chromosomes of each clone, excluding chromosome 10, following the method of Muenzner and colleagues (18). Bottom 30% of least expressed genes were excluded to reduce the noise from the lowly expressed genes in the analysis. Results were plotted on a density plot in $\log_2$ scale, for both mRNA and protein levels, and compared with expected DNA levels. To produce the line plot, the averaged expression (including genes residing on diploid and amplified chromosomes) of each clone was calculated, and the line equation was obtained using linear regression. The distance from the expected equation (DNA content) and the mRNA and protein equations shows dosage compensation. All analyses were performed using Seaborn, Mathplotlib, and Scipy Python packages, statistical analysis was performed using the Mann–Whitney test.

Genes and proteins implicated in the formation of protein complexes were identified using the CORUM database (23). Expression of each gene (protein abundance or DI) was normalized to the expression level in pseudo-diploid clone SS48. Results were plotted in a density plot, separating proteins that are included or not in the CORUM protein complexes. For proteomics, separate analyses for genes localized on diploid and amplified chromosomes were performed. Statistical analysis was performed using the Mann–Whitney test.

miRNA Profiling

miRNA profiling was obtained and performed as previously described in Zerbib and colleagues (14). Briefly, small RNA-seq (sRNA-seq) library was prepared using 1,000 ng of total RNA with the TruSeq Small RNA Kit (Illumina), following the manufacturer's protocol. Sequencing was performed on an Illumina Novaseq 6000 and sequencing quality was checked in the FASTQC report, and only experiments with Q30 or above were considered (Phred Quality Score). Raw data together with a detailed description of the procedures are available in the Gene Expression Omnibus (GEO) database under accession number GSE247267, and the output table is available in Zerbib and colleagues (14).

To study the impact of miRNAs on mRNA expression, a list of differentially downregulated mRNA and differentially upregulated miRNAs relative to SS48 was generated from the RNA-seq and miRNA-seq data. To generate both lists, only the genes significantly (q-value ≤ 0.25) were differentially expressed ($\log_2$ fold change ≥ 1) were included. Both lists were crossed to identify the downregulated mRNAs due to the upregulated miRNAs. Venn diagrams and statistics were performed using Python.

Total RNA Electrophoresis

RNA was harvested from one million cells using Bio-TRI (BioLabs) following the manufacturer's protocol. RNA was run in 1% agarose gel in a cleaned chamber, and migration was imaged every 20 minutes. Smear quantification was performed using ImageJ, by quantifying the smear between the 28S and 16S bands, relative to the total amount of RNA.

Genome-Wide CRISPR Screens and Data Analysis

CRISPR dependency scores (CERES scores) were obtained from Zerbib and colleagues (14). Dependency analysis was performed as previously described in Zerbib and colleagues (14), by a pre-ranked GSEA on the differentially expressed genes using GSEA software 4.0.3, with the following parameters: 1,000 permutations and collapse analysis, using the Hallmark, KEGG, Biocarta, and Reactome gene sets (in separate analyses).

Dependency Map Data Analysis

Extension of the ASs table of each cancer cell line was obtained from Zerbib and colleagues (14). mRNA gene expression values, CRISPR and RNAi dependency scores (Chronos and DEMETER2 scores, respectively) were obtained from DepMap 22Q1 release (https://figshare.com/articles/dataset/DepMap_22Q1_Public/19139906) and compared between the bottom (AS ≤ 8) and top (AS ≥ 21) aneuploidy quartiles.

Doubling time (DT) analyses were performed as previously described in Zerbib and colleagues (14). Briefly, using the extended AS table, and within the bottom (AS ≤ 8) and the top quartile (AS ≥ 21), the DT of each cancer cell line (55) was correlated to gene expression utilizing a linear model following the method of Taylor and colleagues (56). Genes were determined as overexpressed in highly proliferative aneuploid cancer cells if they were significantly associated with DT within the top AS quartile but not within the bottom AS quartile. Significance thresholds: [$\log_{10}(P$ value) ≥ 2.5] OR [$-\log_{10}(P$ value) ≥ 1.3 AND correlation coefficient < −0.005]. The resultant list of genes is available as a supplementary table in Zerbib and colleagues (14). This list was subjected to GSEA using the "Hallmark," "KEGG," "Reactome," and "Gene Ontology Biological Processes" gene set collections from MSigDB (http://www.gsea-msigdb.org/gsea/msigdb/; refs. 17, 57).

qRT-PCR

Cells were harvested using Bio-TRI (Bio-Lab) and RNA was extracted following manufacturer's protocol. cDNA was amplified using the GoScript Reverse Transcription System (Promega) following the manufacturer's protocol. qRT-PCR was performed using SYBR Green, and quantification was performed using the ΔCT method. To estimate RNA degradation rate, cells were treated with 5-μg/mL actinomycin D for 30′ for cJun, 1 hour for *EGR1*, or 3 hours for *KIF18a* and *PLK4*, harvested with Bio-TRI, and the mRNA abundance was assessed for several mRNAs with a short half-life (*cJUN*, *EGR1*, *KIF18A*, and *PLK4*). All primer sequences are available in Supplementary Table S5.

NMD Pathway Reporter Assay

NMD pathway reporter assay was performed as previously described (25). Briefly, 300,000 cells were seeded in six-well plates and transfected 24 hours later with 2 μg of pBS-[CBR-TCR(PTC)]-[CBG-TCR(WT)] plasmid (25) using *Trans*IT-LT1 (Mirus, MIR2300), following manufacturer's protocol. The medium was replaced 24 hours post-transfection. Seventy-two hours post-transfection, RNA was harvested from the treated cells using Bio-TRI (BioLabs) following the manufacturer's protocol. RNA was cleaned from plasmid contamination using TURBO DNA-free Kit (Invitrogen, AM1907), following the manufacturer's protocol. cDNA was amplified using GoScript Reverse Transcription System (Promega), following the manufacturer's protocol. qRT-PCR was performed using Sybr green, and quantification was performed as previously described (25).

Drug Treatments

Drug treatments were performed as previously described in Zerbib and colleagues (14). Briefly, cells were seeded in a 96-well plate using Multidrop Combi Reagent Dispenser (Thermo Fisher Scientific) and then treated 24 hours later with drugs of interest. Alternatively, following aneuploidy induction, cells were washed with PBS to remove reversine, and drugs were applied ~4 hours after seeding the cells. Cell viability was measured at the indicated time point using the MTT assay (Sigma M2128). Formazan crystals were extracted using 10% Triton X-100 and 0.1N HCl in isopropanol, and color absorption was quantified at 570 and 630 nm. EC_{50} for each drug was calculated using GraphPad PRISM 9.1, inhibitor *versus* response (four parameters) nonlinear regression model.

Validation of bortezomib treatment was performed on five near-euploid (CAL51, EN, MHHNB11, SW48, and VMCUB1) and five highly aneuploid (MDA-MB-468, NCIH1693, PANC0813, SH10TC, and A101D) cancer cell lines. Cells were seeded in a 96-well plate, and treated 24 hours later with various concentrations of bortezomib. Cell viability was measured after 72 hours using CellTiter-Glo (Promega). EC_{50} was calculated using GraphPad PRISM 8, an asymmetric (five-parameter) nonlinear regression model. In Supplementary Fig. S8M, CAL51 and MDA-MB-468 were imaged after 72 hours of exposure to bortezomib, using Incucyte (Sartorius). For visualization, the cell borders were highlighted using an AI-trained Ilastik software. All drug details are available in Supplementary Table S5.

Flow Cytometry Analyses

RPE1 clones were seeded and treated with 20 nmol/L ouabain or 2.4 nmol/L bortezomib for 48 hours. For cell death assessment, cells were washed and live-stained with Annexin V/PI (#640930, BioLegend), following the manufacturer's protocol. For cell cycle, cells were fixed using ice-cold 70% ethanol for 2 hours on ice and then stained with 50 μg/mL propidium iodine (BioLegend) and 0.1 mg/mL RNAse A (Invitrogen) in PBS for 10 minutes at room temperature. Flow cytometry acquisition was performed on CytoFLEX (Beckman Coulter) and data analysis was performed using CytExpert v2.4 analysis software (Beckman Coulter). The same gating of live single cells was applied across all the analyzed samples, whereas the gating of the cell cycle phase was specific to each clone.

siRNA Transfection

Cells were transfected with siRNAs against *CASC3*, *DROSHA*, *PRKRA*, or *TARBP2* (ONTARGETplus SMART-POOL, Dharmacon; individual oligos, Sigma-Aldrich) or with a control siRNA (ONTARGETplus SMART-POOL, Dharmacon; non-targeting siRNA, Sigma-Aldrich) using Lipofectamine RNAiMAX (Invitrogen), following manufacturers' protocols. To test whether aneuploidy induction sensitized cells to CASC3, cells were seeded and synchronized with thymidine 5 mmol/L for 24 hours and then treated with reversine 500 nmol/L for 20 hours. After the reversine pulse, cells were reverse-transfected with siRNA against *CASC3* using Lipofectamine RNAiMAX, following the manufacturer's protocol. Cell growth following siRNA transfection was followed by live cell imaging using Incucyte (Sartorius). The effect of the knockdown on viability was calculated by comparing the cell number in the targeted siRNA *versus* control siRNA wells at 72 hours post-transfection. All oligo details are listed in Supplementary Table S5.

Western Blot

Cells were lysed in NP-40 lysis buffer (1% NP-40;150 mmol/L NaCl; 50-mmol/L Tris HCl pH 8.0) with the addition of protease inhibitor cocktail (Sigma-Aldrich #P8340) and phosphatase inhibitor cocktail (Sigma-Aldrich #P0044). Protein lysates were sonicated (Biorector) for 5 minutes (30 seconds on/30 seconds off) at 4°C and then centrifuged at maximum speed for 15 minutes and resolved on 12% SDS-PAGE gels. Bands were detected using chemoluminescence (Millipore #WBLUR0500) on Fusion FX gel-doc (Vilber). For the SUnSET puromycin incorporation assay, cells were treated with 10-μg/mL puromycin for 30 minutes prior to harvest. All antibodies are listed and their use is described in Supplementary Table S5.

Proteasome Activity Assay

Proteasome activity was estimated using Proteasome-Glo Chemotrypsin-like kit (Promega), following the manufacturer's protocol. Briefly, cells were trypsinized and washed twice with medium to remove residual trypsin. A total of 4,000 cells were seeded in triplicate in a white 96-well plate and incubated for 2 hours at 37°C. Thirty-minute exposure to 1 μmol/L of bortezomib was used as a positive control for proteasome activity inhibition. The plate was shaken for 2 minutes at high speed and incubated for 5 minutes at room temperature, and luminescence was then measured using a Synergy H1 plate reader (BioTEK).

PRISM Screen

PRISM screen was performed as previously described (38, 39). Briefly, cells were plated in triplicate in 384-well plates at 1,250 cells per well. Cells were treated with the proteasome inhibitor bortezomib (eight concentrations of threefold dilutions, ranging from 91 nmol/L to 20 μmol/L) in the presence of reversine (250 nmol/L) or DMSO for 5 days. Cells were then lysed, and lysate plates were pooled for amplification and barcode measurement. Viability values were calculated by taking the median fluorescence intensity of beads corresponding to each cell line barcode and normalizing them by the median of DMSO control. Dose–response curves and EC_{50} values were calculated by fitting four-parameter curves to viability data for each cell line, using the R drc package, fixing the upper asymptote of the logistic curves to 1. EC_{50} comparisons were performed on the 387 cell lines for which well-fit curves ($r^2 > 0.3$) were generated.

TCGA Data Analysis

TCGA data were retrieved using the TCGAbiolinks R package (58). ASs were obtained from Taylor and colleagues (56) and correlated to tumor gene expression using lineage as a covariate (lm function in R studio v4.1.1, using the equation: gene ~ AS+lineage), as previously described (56). Genes were ranked based on their AS coefficient, and then subjected to pre-ranked GSEA (17) using the "Hallmark," "Biocarta," "KEGG," and "Reactome" gene set collections from MSigDB.

Analyses of Data from Clinical Trials

Raw SNP6 CEL, gene expression, and response data were obtained from the GEO database for monotherapy (ref. 42; GSE9782) or combination therapies (refs. 43, 44; GSE159426 and GSE69028) multiple myeloma clinical trials. For the monotherapy trial (42), the CAFE algorithm (41) v1.34.0 was used to assess the chromosome arm AS for each patient, with the armStats function and default parameters were used to identify significant chromosome arm losses and gains (Bonferroni adjusted P value < 0.05). For the combination therapy trial GSE159426 (43), gene expression was quantified using Kallisto (59), and gene-level copy number variation (CNV) was inferred from the gene expression using CNVkit (60). For the combination therapy trial GSE69028 (44), the segmented copy number calls for each patient were estimated using Rawcopy (61) v1.1 from the raw SNP6 CEL files, using default parameters. For both combination therapy trials, ASs were calculated using ASCETS (62). For all clinical trials, the inferred ASs were compared between the "non-responders" (progressive disease, stable disease, or minimal response) and the "responders" (complete response) patients.

Drug response data of the metastatic PDAC PDX cohort (45) was obtained from the EMBL-EBI database (E-MAT-5039). Gene expression was quantified using Kallisto (59) and gene-level CNV was inferred from the gene expression using CNVkit (60). Aneuploidy scores were calculated by calculating the number of chromosome arms that deviate from basal ploidy using ASCETS (62), with a cutoff of $|\log_2(\text{CNV})| > 0.3$. Drug response data from the pediatric PDX cohort was obtained (EA00001002528) and tumors were separated based on their response to drugs of interest as previously described (46). Copy number calling was performed using the CONSERTING algorithm (63) and kindly provided by Dr. Jiyang Yu. Linear regression analysis to assess the relationship between the AUC (dependent variable) and AS (independent variable) was performed using the Statsmodel Python package.

Statistical Analyses

The number of cells used for each experiment is available in the method section. Western Blot quantifications were performed using ImageJ and Image Lab. The numbers of independent experiments and analyzed cell lines of each computational analysis are available in the figure legends. Statistical analyses were performed using GraphPad PRISM 9.1. Details of each statistical test are indicated in the figure legends. In each presented box plot, the internal bar represents the median of the distribution. In Fig. 1C and F, the bar represents the mean ± SEM. Significance thresholds were defined as P value = 0.05 and q-value = 0.25.

Data Availability

Aneuploid RPE1-hTERT clones generated in this study are available upon request to Stefano Santaguida. Raw RNA-seq data are available in the SRA database (https://www.ncbi.nlm.nih.gov/sra) under accession number PRJNA889550 (RPE1-hTERT clones) or PRJNA1097018 (aneuploidy-induced HCT116). miRNA sequencing data and proteomics of RPE1-hTERT clones are available in the GEO database (GSE247267) and the PRIDE database (PXD048833), respectively. Genome-wide CRISPR/Cas9 screening data of RPE1-hTERT clones are available in the DepMap database 21Q3 release (https://figshare.com/articles/dataset/DepMap_21Q3_Public/15160110). Cancer cell line expression, CRISPR/Cas9, and RNAi data are available in the DepMap database 22Q1 release (https://figshare.com/articles/dataset/DepMap_22Q1_Public/19139906). Aneuploidy scores of cancer cell lines are available in Zerbib and colleagues (14).

Authors' Disclosures

U. Ben-David reports grant funding from Novocure and consulting fees from Accent Therapeutics. E. Ruppin is a cofounder of MedAware, Metabomed, and Pangea Biomed (divested), as well as an unpaid member of Pangea Biomed's Scientific Advisory Board. F. Vazquez reports research support from the Dependency Map Consortium, Riva Therapeutics, Bristol Myers Squibb, Merck, Illumina, and Deerfield Management; being on the Scientific Advisory Board of GSK; and holding equity and is a consultant for Riva Therapeutics and Jumble Therapeutics. No disclosures were reported by the other authors.

Authors' Contributions

U. Ben-David and **S. Santaguida** jointly conceived the study, directed and supervised it. **J. Zerbib** and **M.R. Ippolito** jointly designed and performed most of the experiments. **J. Zerbib**, **M.R. Ippolito**, **U. Ben-David**, and **S. Santaguida** analyzed the data with inputs from all co-authors. **Y. Eliezer** and **E. Reuveni**, **E.D. Shulman**, **T. Chang**, **E.M. Campangnolo**, **T. Ben-Yishay**, and **E. Ruppin** assisted with bioinformatic analyses. **S. Viganò**, **G. De Feudis**, **A. Savir Kadmon**, **R. Slutsky**, **S. Taglietti**, **S. Scorzoni**, **S. Gianotti**, **S. Martin**, **K. Laue**, **J. Muenzner**, **M. Mülleder**, **N. Rozenblum**, **F. Nicassio**, **M. Ralser**, **Y. Cohen-Sharir**, and **I. Vigorito** assisted with *in vitro* experiments. **F. Vazquez** directed the genomic profiling and CRISPR screens. **J. Zerbib**, **M.R. Ippolito**, **U. Ben-David**, and **S. Santaguida** wrote the manuscript with inputs from all co-authors.

Acknowledgments

The authors would like to thank James McFarland and Ofir Hameiri for their bioinformatic support; Gil Ast, Marina Mapelli, Zuzana Tothova, and members of the U. Ben-David and S. Santaguida labs for helpful discussions; Varda Wexler for assistance with figure preparation; Zuzana Storchova for providing the RPE1/RPT cell lines; Zhongsheng You for providing the NMD reporter constructs; and Nicholas Lyons, Jordan Bryan, Samantha Bender, and Jennifer Roth for their assistance with the PRISM screen. We thank the Broad Institute Genomic Perturbation Platform for their assistance with the CRISPR–Cas9 screens. This work was supported by the European Research Council Starting Grant (grant #945674 to U. Ben-David), the Israel Cancer Research Fund Project Award (U. Ben-David), the Azrieli Foundation Faculty Fellowship (U. Ben-David), the DoD CDMRP Career Development Award (grant #CA191148 to U. Ben-David), the Israel Science Foundation (grant #1805/21 to U. Ben-David), the BSF project grant (grant #2019228 to U. Ben-David), the Italian Association for Cancer Research (AIRC-MFAG 2018—ID. 21665 and Bridge Grant 2023—ID. 29228 projects to S. Santaguida), Ricerca Finalizzata (GR-2018–12367077 to S. Santaguida), Fondazione Cariplo (S. Santaguida), the Rita-Levi Montalcini program from MIUR (to S. Santaguida), and the Italian Ministry of Health with Ricerca Corrente and 5x1000 funds (S. Santaguida). U. Ben-David is an EMBO Young Investigator. J. Zerbib was supported by fellowships from the Israeli Ministry for Immigrant Absorption, the Pfizer-Wexler Excellence Scholarship, and the Yoran Institute for Human Genome Research and by travel awards from the TAU Constantiner Institute and Cancer Biology Research Center. M.R. Ippolito is supported by an AIRC Fellowship (ID 26738-2021). J. Zerbib, R. Slutsky, and Y. Eliezer

are PhD and MD-PhD students within the graduate school of the Faculty of Medicine, Tel Aviv University. T. Ben-Yishay was supported in part by a fellowship from the Edmond J. Safra Center for Bioinformatics at Tel Aviv University. M.R. Ippolito, S. Martin, S. Viganò, and S. Scorzoni are PhD students at the European School of Molecular Medicine.

Note

Supplementary data for this article are available at Cancer Discovery Online (http://cancerdiscovery.aacrjournals.org/).

Received March 15, 2023; revised April 10, 2024; accepted August 2, 2024; published first September 9, 2024.

REFERENCES

1. Kojima S, Cimini D. Aneuploidy and gene expression: is there dosage compensation? Epigenomics 2019;11:1827–37.
2. Donnelly N, Passerini V, Dürrbaum M, Stingele S, Storchová Z. HSF 1 deficiency and impaired HSP 90-dependent protein folding are hallmarks of aneuploid human cells. EMBO J 2014;33:2374–87.
3. Gonçalves E, Fragoulis A, Garcia-Alonso L, Cramer T, Saez-Rodriguez J, Beltrao P. Widespread post-transcriptional attenuation of genomic copy-number variation in cancer. Cell Syst 2017;5:386–98.e4.
4. Schukken KM, Sheltzer JM. Extensive protein dosage compensation in aneuploid human cancers. Genome Res 2022;32:1254–70.
5. Senger G, Santaguida S, Schaefer MH. Regulation of protein complex partners as a compensatory mechanism in aneuploid tumors. Elife 2022;11:e75526.
6. Cheng P, Zhao X, Katsnelson L, Camacho-Hernandez EM, Mermerian A, Mays JC, et al. Proteogenomic analysis of cancer aneuploidy and normal tissues reveals divergent modes of gene regulation across cellular pathways. Elife 2022;11:e75227.
7. Torres EM, Sokolsky T, Tucker CM, Chan LY, Boselli M, Dunham MJ, et al. Effects of aneuploidy on cellular physiology and cell division in haploid yeast. Science 2007;317:916–24.
8. Torres EM, Dephoure N, Panneerselvam A, Tucker CM, Whittaker CA, Gygi SP, et al. Identification of aneuploidy-tolerating mutations. Cell 2010;143:71–83.
9. Dephoure N, Hwang S, O'Sullivan C, Dodgson SE, Gygi SP, Amon A, et al. Quantitative proteomic analysis reveals posttranslational responses to aneuploidy in yeast. Elife 2014;3:e03023.
10. Oromendia AB, Dodgson SE, Amon A. Aneuploidy causes proteotoxic stress in yeast. Genes Dev 2012;26:2696–708.
11. Pavelka N, Rancati G, Zhu J, Bradford WD, Saraf A, Florens L, et al. Aneuploidy confers quantitative proteome changes and phenotypic variation in budding yeast. Nature 2010;468:321–5.
12. Torres EM, Springer M, Amon A. No current evidence for widespread dosage compensation in S. cerevisiae. Elife 2016;5:e10996.
13. Mohanty V, Wang F, Mills GB; CTD2 Research Network, Chen K. Uncoupling of gene expression from copy number presents therapeutic opportunities in aneuploid cancers. Cell Rep Med 2021;2:100349.
14. Zerbib J, Ippolito MR, Eliezer Y, De Feudis G, Reuveni E, Kadmon AS, et al. Human aneuploid cells depend on the RAF/MEK/ERK pathway for overcoming increased DNA damage. Nat Commun 2024;15:7772.
15. Santaguida S, Tighe A, D'Alise AM, Taylor SS, Musacchio A. Dissecting the role of MPS1 in chromosome biorientation and the spindle checkpoint through the small molecule inhibitor reversine. J Cell Biol 2010;190:73–87.
16. Santaguida S, Vasile E, White E, Amon A. Aneuploidy-induced cellular stresses limit autophagic degradation. Genes Dev 2015;29:2010–21.
17. Subramanian A, Tamayo P, Mootha VK, Mukherjee S, Ebert BL, Gillette MA, et al. Gene set enrichment analysis: a knowledge-based approach for interpreting genome-wide expression profiles. Proc Natl Acad Sci U S A 2005;102:15545–50.
18. Muenzner J, Trébulle P, Agostini F, Zauber H, Messner CB, Steger M, et al. Natural proteome diversity links aneuploidy tolerance to protein turnover. Nature 2024;630:149–57.
19. Dürrbaum M, Kruse C, Nieken KJ, Habermann B, Storchová Z. The deregulated microRNAome contributes to the cellular response to aneuploidy. BMC Genomics 2018;19:197.
20. Yahya G, Menges P, Amponsah PS, Ngandiri DA, Schulz D, Wallek A, et al. Sublinear scaling of the cellular proteome with ploidy. Nat Commun 2022;13:6182.
21. Stingele S, Stoehr G, Peplowska K, Cox J, Mann M, Storchova Z. Global analysis of genome, transcriptome and proteome reveals the response to aneuploidy in human cells. Mol Syst Biol 2012;8:608.
22. Xiong B, Yang Y, Fineis FR, Wang J-P. DegNorm: normalization of generalized transcript degradation improves accuracy in RNA-seq analysis. Genome Biol 2019;20:75.
23. Tsitsiridis G, Steinkamp R, Giurgiu M, Brauner B, Fobo G, Frishman G, et al. CORUM: the comprehensive resource of mammalian protein complexes–2022. Nucleic Acids Res 2023;51:D539–45.
24. Wang M, Zhang P, Zhu Y, Kong X, Zhang Z, Hu L. Assessing the activity of nonsense-mediated mRNA decay in lung cancer. BMC Med Genomics 2017;10:55.
25. Nickless A, Jackson E, Marasa J, Nugent P, Mercer RW, Piwnica-Worms D, et al. Intracellular calcium regulates nonsense-mediated mRNA decay. Nat Med 2014;20:961–6.
26. Gerbracht JV, Boehm V, Britto-Borges T, Kallabis S, Wiederstein JL, Ciriello S, et al. CASC3 promotes transcriptome-wide activation of nonsense-mediated decay by the exon junction complex. Nucleic Acids Res 2020;48:8626–44.
27. Azzalin CM, Reichenbach P, Khoriauli L, Giulotto E, Lingner J. Telomeric repeat-containing RNA and RNA surveillance factors at mammalian chromosome ends. Science 2007;318:798–801.
28. Brumbaugh KM, Otterness DM, Geisen C, Oliveira V, Brognard J, Li X, et al. The mRNA surveillance protein hSMG-1 functions in genotoxic stress response pathways in mammalian cells. Mol Cell 2004;14:585–98.
29. Melamed Z, Levy A, Ashwal-Fluss R, Lev-Maor G, Mekahel K, Atias N, et al. Alternative splicing regulates biogenesis of miRNAs located across exon-intron junctions. Mol Cell 2013;50:869–81.
30. Ohashi A, Ohori M, Iwai K, Nakayama Y, Nambu T, Morishita D, et al. Aneuploidy generates proteotoxic stress and DNA damage concurrently with p53-mediated post-mitotic apoptosis in SAC-impaired cells. Nat Commun 2015;6:7668.
31. Ben-David U, Amon A. Context is everything: aneuploidy in cancer. Nat Rev Genet 2020;21:44–62.
32. Zhu J, Tsai H-J, Gordon MR, Li R. Cellular stress associated with aneuploidy. Dev Cell 2018;44:420–31.
33. Hetz C, Zhang K, Kaufman RJ. Mechanisms, regulation and functions of the unfolded protein response. Nat Rev Mol Cell Biol 2020;21:421–38.
34. Kuznetsova AY, Seget K, Moeller GK, de Pagter MS, de Roos JADM, Dürrbaum M, et al. Chromosomal instability, tolerance of mitotic errors and multidrug resistance are promoted by tetraploidization in human cells. Cell Cycle 2015;14:2810–20.
35. Schmidt EK, Clavarino G, Ceppi M, Pierre P. SUnSET, a nonradioactive method to monitor protein synthesis. Nat Methods 2009;6:275–7.
36. Xian S, Dosset M, Almanza G, Searles S, Sahani P, Waller TC, et al. The unfolded protein response links tumor aneuploidy to local immune dysregulation. EMBO Rep 2021;22:e52509.
37. Santaguida S, Amon A. Short- and long-term effects of chromosome mis-segregation and aneuploidy. Nat Rev Mol Cell Biol 2015;16:473–85.
38. Cohen-Sharir Y, McFarland JM, Abdusamad M, Marquis C, Bernhard SV, Kazachkova M, et al. Aneuploidy renders cancer cells vulnerable to mitotic checkpoint inhibition. Nature 2021;590:486–91.
39. Corsello SM, Nagari RT, Spangler RD, Rossen J, Kocak M, Bryan JG, et al. Discovering the anticancer potential of non-oncology drugs by systematic viability profiling. Nat Cancer 2020;1:235–48.

40. Ben-David U, Mayshar Y, Benvenisty N. Virtual karyotyping of pluripotent stem cells on the basis of their global gene expression profiles. Nat Protoc 2013;8:989–97.
41. Bollen S, Leddin M, Andrade-Navarro MA, Mah N. CAFE: an R package for the detection of gross chromosomal abnormalities from gene expression microarray data. Bioinformatics 2014;30:1484–5.
42. Mulligan G, Mitsiades C, Bryant B, Zhan F, Chng WJ, Roels S, et al. Gene expression profiling and correlation with outcome in clinical trials of the proteasome inhibitor bortezomib. Blood 2007;109:3177–88.
43. Borisov N, Sergeeva A, Suntsova M, Raevskiy M, Gaifullin N, Mendeleeva L, et al. Machine learning applicability for classification of PAD/VCD chemotherapy response using 53 multiple myeloma RNA sequencing profiles. Front Oncol 2021;11:652063.
44. Terragna C, Remondini D, Martello M, Zamagni E, Pantani L, Patriarca F, et al. The genetic and genomic background of multiple myeloma patients achieving complete response after induction therapy with bortezomib, thalidomide and dexamethasone (VTD). Oncotarget 2016;7:9666–79.
45. Fraunhoffer NA, Abuelafia AM, Bigonnet M, Gayet O, Roques J, Telle E, et al. Evidencing a pancreatic ductal adenocarcinoma subpopulation sensitive to the proteasome inhibitor carfilzomib. Clin Cancer Res 2020;26:5506–19.
46. Stewart E, Federico SM, Chen X, Shelat AA, Bradley C, Gordon B, et al. Orthotopic patient-derived xenografts of paediatric solid tumours. Nature 2017;549:96–100.
47. Torres EM, Williams BR, Amon A. Aneuploidy: cells losing their balance. Genetics 2008;179:737–46.
48. Hwang S, Cavaliere P, Li R, Zhu LJ, Dephoure N, Torres EM. Consequences of aneuploidy in human fibroblasts with trisomy 21. Proc Natl Acad Sci U S A 2021;118:e2014723118.
49. Passerini V, Ozeri-Galai E, De Pagter MS, Donnelly N, Schmalbrock S, Kloosterman WP, et al. The presence of extra chromosomes leads to genomic instability. Nat Commun 2016;7:10754.
50. Chunduri NK, Menges P, Zhang X, Wieland A, Gotsmann VL, Mardin BR, et al. Systems approaches identify the consequences of monosomy in somatic human cells. Nat Commun 2021;12:5576.
51. Love MI, Huber W, Anders S. Moderated estimation of fold change and dispersion for RNA-seq data with DESeq2. Genome Biol 2014;15:550.
52. Tapial J, Ha KCH, Sterne-Weiler T, Gohr A, Braunschweig U, Hermoso-Pulido A, et al. An atlas of alternative splicing profiles and functional associations reveals new regulatory programs and genes that simultaneously express multiple major isoforms. Genome Res 2017;27:1759–68.
53. Demichev V, Messner CB, Vernardis SI, Lilley KS, Ralser M. DIA-NN: neural networks and interference correction enable deep proteome coverage in high throughput. Nat Methods 2020;17:41–4.
54. UniProt Consortium; Bateman A, Martin M-J, Orchard S, Magrane M, Agivetova R, Ahmad S, et al. UniProt: the universal protein knowledgebase in 2021. Nucleic Acids Res 2021;49:D480–9.
55. Tsherniak A, Vazquez F, Montgomery PG, Weir BA, Kryukov G, Cowley GS, et al. Defining a cancer dependency Map. Cell 2017;170:564–76.e16.
56. Taylor AM, Shih J, Ha G, Gao GF, Zhang X, Berger AC, et al. Genomic and functional approaches to understanding cancer aneuploidy. Cancer Cell 2018;33:676–89.e3.
57. Liberzon A, Birger C, Thorvaldsdóttir H, Ghandi M, Mesirov JP, Tamayo P. The Molecular Signatures Database (MSigDB) hallmark gene set collection. Cell Syst 2015;1:417–25.
58. Colaprico A, Silva TC, Olsen C, Garofano L, Cava C, Garolini D, et al. TCGAbiolinks: an R/Bioconductor package for integrative analysis of TCGA data. Nucleic Acids Res 2016;44:e71.
59. Bray NL, Pimentel H, Melsted P, Pachter L. Near-optimal probabilistic RNA-seq quantification. Nat Biotechnol 2016;34:525–7.
60. Talevich E, Shain AH, Botton T, Bastian BC. CNVkit: genome-wide copy number detection and visualization from targeted DNA sequencing. PLoS Comput Biol 2016;12:e1004873.
61. Mayrhofer M, Viklund B, Isaksson A. Rawcopy: improved copy number analysis with Affymetrix arrays. Sci Rep 2016;6:36158.
62. Spurr LF, Touat M, Taylor AM, Dubuc AM, Shih J, Meredith DM, et al. Quantification of aneuploidy in targeted sequencing data using ASCETS. Bioinformatics 2021;37:2461–3.
63. Chen X, Gupta P, Wang J, Nakitandwe J, Roberts K, Dalton JD, et al. CONSERTING: integrating copy number analysis with structural variation detection. Nat Methods 2015;12:527–30.